Monthly Notices
of the
ROYAL ASTRONOMICAL SOCIETY

MNRAS **478,** 4952–4973 (2018) doi:10.1093/mnras/sty991

Exploring relations between BCG and cluster properties in the SPectroscopic IDentification of eROSITA Sources survey from $0.05 < z < 0.3$

Kate E. Furnell,[1★] Chris A. Collins,[1] Lee S. Kelvin,[1] Nicolas Clerc,[2,3] Ivan K. Baldry,[1] Alexis Finoguenov,[2,4] Ghazaleh Erfanianfar,[2] Johan Comparat[2] and Donald P. Schneider[5,6]

[1]*Astrophysics Research Institute, Liverpool John Moores University, IC2, Liverpool Science Park, 146 Brownlow Hill, Liverpool, L3 5RF, UK*
[2]*High-Energy Astrophysics Group, Max Planck Institute for Extraterrestrial Physics, Giessenbachstrasse, D-85741 Garching, Germany*
[3]*IRAP, Université de Toulouse, CNRS, UPS, CNES, Toulouse, France*
[4]*Department of Physics, University of Helsinki, PL 64 (Gustaf Hällströmin Katu 2), FI-D318, Helsinki, Finland*
[5]*Department of Astronomy and Astrophysics, The Pennsylvania State University, University Park, PA 16802, USA*
[6]*Institute for Gravitation and the Cosmos, The Pennsylvania State University, University Park, PA 16802, USA*

Accepted 2018 March 28. Received 2018 March 9; in original form 2017 December 1

ABSTRACT

We present a sample of 329 low-to intermediate-redshift ($0.05 < z < 0.3$) brightest cluster galaxies (BCGs) in X-ray-selected clusters from the SPectroscopic IDentification of eRosita Sources survey, a spectroscopic survey within Sloan Digital Sky Survey-IV (SDSS-IV). We define our BCGs by simultaneous consideration of legacy X-ray data from *ROSAT*, maximum-likelihood outputs from an optical cluster-finder algorithm and visual inspection. Using SDSS imaging data, we fit Sérsic profiles to our BCGs in three bands (g, r, i) with SIGMA a GALFIT-based software wrapper. We examine the reliability of our fits by running our pipeline on $\sim 10^4$ point spread function-convolved model profiles injected into eight random cluster fields; we then use the results of this analysis to create a robust subsample of 198 BCGs. We outline three cluster properties of interest: overall cluster X-ray luminosity (L_X), cluster richness as estimated by REDMAPPER (λ),and cluster halo mass (M_{200}), which is estimated via velocity dispersion. In general, there are significant correlations with BCG stellar mass between all three environmental properties, but no significant trends arise with either Sérsic index or effective radius. There is no major environmental dependence on the strength of the relation between effective radius and BCG stellar mass. Stellar mass therefore arises as the most important factor governing BCG morphology. Our results indicate that our sample consists of a large number of relaxed, mature clusters containing broadly homogeneous BCGs up to $z \sim 0.3$, suggesting that there is little evidence for much ongoing structural evolution for BCGs in these systems.

Key words: galaxies: clusters: general – galaxies: elliptical and lenticular, cD – galaxies: evolution – galaxies: structure.

1 INTRODUCTION

Galaxy clusters, the nodes of the cosmic web, are the largest gravitationally bound structures in our Universe, most of which host a massive 'brightest cluster galaxy', or BCG, at their core. BCGs are unique objects, thought to represent a distinct population (Djorgovski & Davis 1987) separate from the general elliptical non-BCG population (von der Linden et al. 2007) The visual distinctions are often pronounced at local scales, with many BCGs hosting distinct, extended envelopes of stars (e.g. Morgan & Lesh 1965; Schombert 1986). They also exhibit extraordinary homogeneity, with many studies finding uniformly luminous BCGs in similarly massive clusters up to redshifts of $z \sim 1$ (Aragon-Salamanca, Baugh & Kauffmann 1998; Collins et al. 2009; Whiley et al. 2008). This property conflicts with current simulations, which struggle to reproduce the observed homogeneity seen in BCGs up to redshifts of $z \sim 1$. Many simulations are successful in reproducing the colours

★ E-mail: K.E.Furnell@2015.ljmu.ac.uk

of observed BCGs, but they fail to accurately model BCG growth, overpredicting the observed amount by between a factor of 2–4 (e.g. De Lucia & Blaizot 2007; Ragone-Figueroa et al. 2013). Although improvements have been made in recent years, most simulations still cannot reproduce the observed morphologies of BCGs in general, especially within their central regions (e.g. Laporte & White 2015; Tonini et al. 2012). It has been recognized therefore that understanding the growth of BCGs and the global accumulation of baryons in cluster cores may be critical for solving some of the discrepancies suffered by clusters in hydrodynamical simulations, such as the well-documented cuspy halo problem (e.g. Navarro, Frenk & White 1996).

In contrast to nearby clusters, identifying the BCG is often non-trivial in more distant clusters. It has been established for some time that, for the majority of galaxy clusters which are dynamically 'relaxed', BCGs reside close to the peak of cluster X-ray emission (e.g. Lin & Mohr 2004; Hudson et al. 2010). This X-ray peak signifies inflow of the intracluster medium (ICM), the hot, diffuse gas between clusters, into the cluster core; this is indicative of a deep potential well (e.g. Lea et al. 1973; Fabian & Nulsen 1977). However, for clusters out of dynamic equilibrium (i.e. ones which have undergone recent mergers with neighbouring groups), this technique is ineffective, with multiple, similarly luminous candidate BCGs and X-ray peaks often being present (e.g. Markevitch et al. 2002). Merger activity is more common in high-redshift systems, leading many to conclude that hierarchical merging is the dominant mechanism behind the growth of galaxy clusters (e.g. White & Frenk 1991). Nevertheless, there are many issues to consider when quantifying cluster parameters such as mass, with numerous proxies used throughout the literature with various caveats (e.g. caustics, velocity dispersions, richnesses, X-ray mass–temperature scaling, and weak gravitational lensing; see Old et al. 2015).

Due to the location of BCGs at the peak of X-ray emission in relaxed clusters, there is speculation that BCGs predominantly grow through ongoing star formation as a result of condensing cluster gas regulated by some feedback mechanism (Fabian et al. 1994; McNamara et al. 2014; Voit et al. 2016). For many hydrodynamical simulations, active galactic nucleus (AGN) activity remains the favoured dominant candidate for feedback (e.g. McCarthy et al. 2016; Schaye et al. 2015; Vogelsberger et al. 2014), although some studies are moving towards closer examination of external baryonic processes, such as ram-pressure stripping and shock heating (e.g. Steinhauser, Schindler & Springel 2016). Indeed, high rates of star formation (10^1–$10^2\,\mathrm{M_\odot yr^{-1}}$) have been detected in some BCGs within clusters hosting cool cores (e.g. O'Dea et al. 2008; Edge 2001) as well as enhanced AGN activity (e.g. Burns 1990) and giant molecular gas outflows (e.g. Russell et al. 2014). However, mass deposition rates may still be too slow to reproduce the mass range of BCGs through *in situ* star formation alone (e.g. Peterson & Fabian 2006), alongside strong cool-core systems being relatively rare at higher redshifts where observations suggest BCGs gain the bulk of their mass (Vikhlinin et al. 2007; Collins et al. 2009).

BCG formation scenarios based on classical hierarchical merging have risen as a popular alternative to growth through star formation since $z \sim 1$ (e.g. Ostriker & Tremaine 1975; Merritt 1985). Broadly, these models fall into two categories: 'galactic merging', where many similarly sized galaxies violently merge together in a short amount of time to form the BCG, or 'galactic cannibalism', a slower process where mass is accumulated over time from smaller galaxies sinking to the bottom of the cluster potential well. Currently, a two-step scenario behind BCG formation is favoured (e.g. Johansson, Naab & Ostriker 2012), with the bulge forming first at early times ($z > 2$) followed by the envelope feature at late times ($z < 1$). This approach has gained popularity as an explanation behind the 'cD-type' morphologies (i.e. bulge + halo) seen in many BCGs at low redshift, as well as the apparent 'puffing up' of elliptical types (e.g. van Dokkum et al. 2008; van der Wel et al. 2008). Indeed, there is convincing indirect evidence that merger events happen at some point in the formation history of BCGs, with many examples of BCGs hosting multiple nuclei at their centres (e.g. Lauer 1988; Schneider, Gunn & Hoessel 1983).

The purpose of this work is to investigate a sample of BCGs in order to examine their properties with respect to the properties of their host clusters. As aforementioned, many studies have found links of varying strength between the properties of BCGs and their host clusters up to redshifts of $z \sim 1$ (e.g. Zhao, Aragón-Salamanca & Conselice 2015b; von der Linden et al. 2007; Stott et al. 2008, 2011). Numerous studies have reported a positive correlation between BCG stellar masses and environmental properties, such as the overall halo mass (e.g. Bhavsar & Barrow 1985; Lin & Mohr 2004 and references therein), with some finding tentative environmental links between various BCG morphological properties and their host clusters (e.g. Brough et al. 2005; Guo et al. 2009). However, others have found little-to-no dependence at low redshift (Zhao et al. 2015b), or have argued that the effect strengthens for central galaxies with late-type morphologies but is not strongly observed in early types (e.g. Weinmann et al. 2009).

In this study, we aim to analyse the light profiles of a sample of BCGs with respect to the global cluster environment. We select three major cluster properties to analyse: dynamically derived halo mass M_{200}, X-ray luminosity L_X, and cluster richness λ, an estimate of overall cluster membership. This paper is structured as follows: in Section 2.2, we discuss the data used in procuring the sample of BCGs used here. In Section 3.1, we discuss our analysis of the host cluster dynamics in our sample and our estimation of halo mass. In Sections 3.2–3.4, we discuss the 2D profile fitting techniques used for our sample, as well as a suite of simulations used to test their reliability and bring to light any potential biases. In Section 4, we describe our results, including a discussion of our method of estimating stellar masses for our objects. We assume a standard Λ cold dark matterconcordance cosmology throughout, with $H_0 = 70$ $\mathrm{km\,s^{-1}\,Mpc^{-1}}$, $h_{100} = 0.7$, $\Omega_\Lambda = 0.7$, and $\Omega_\mathrm{M} = 0.3$.

2 DATA

2.1 Data description

This work makes use of observations primarily from two separate sources: X-ray observations from the ROSAT All-Sky Survey (RASS), a shallow, low signal-to-noise ratio, all-sky survey of soft X-ray sources running between 1990and 1999 (Voges et al. 1999) and optical data from the Sloan Digital Sky Survey (SDSS; York et al. 2000). The spectroscopic data for this work originate from the SDSS-IV (Blanton et al. 2017) SPectroscopic IDentification of eRosita Sources (SPIDERS) survey, which aims to investigate $\sim 10^4$ X-ray targets detectable by eROSITA prior to launch in 2018. eROSITA has been designed with full-sky survey capabilities, with high angular resolution (15arcsec) and has been predicted to detect all clusters in the Universe above $10^{14}\,\mathrm{M_\odot}$ ($\sim$57, 500 clusters out of $\sim$137 000 total group/cluster detections, Pillepich, Porciani & Reiprich 2012), creating the largest and most complete X-ray-selected sample of galaxy clusters to date. Optical spectroscopy for SPIDERS are being performed within the extended Baryon Oscillation Spectroscopic Survey (eBOSS) footprint with the BOSS

spectrograph on the SDSS 2.5 m Apache Point Observatory telescope (e.g. Dawson et al. 2016; Smee et al. 2013; Gunn et al. 2006) and will continue until the end of the project in 2020.

The purpose of the clusters programme in SPIDERS (Clerc et al. 2016) is to obtain observations on a sample of X-ray-selected cluster candidates, in order to procure precise redshift measurements of member galaxies. The subsample of cluster candidates in SPIDERS used for this study originates from the COnstrain Dark Energy with X-ray Clusters (CODEX; Finoguenov et al., in preparation) survey. Essentially, the CODEX survey combines [0.5–2] keV band *ROSAT* X-ray data with optical data from redMaPPer (i.e. the red-sequence Matched-filter Probabilistic Percolation algorithm; see Rykoff et al. 2014), an optical cluster finder search on SDSS DR8 data (e.g. Aihara et al. 2011). In basic terms, the algorithm works through the use of a preliminary 'seed' catalogue of red galaxies with spectroscopic data. These 'seeds' are used to 'train' the algorithm, providing a baseline for photometric redshift estimates. Cluster galaxies are assigned a probability, $P_{\rm MEM}$, of being a member of a detected overdensity of photometrically grouped red galaxies about a given 'seed' galaxy, with the sample undergoing simultaneous filtration in luminosity ($L \geq 0.2L_{\star}$) and projected distance corresponding to the size of a typical cluster at the redshift of the 'seed' galaxy. This approach has been enormously successful in both the SDSS and the Dark Energy Survey (The Dark Energy Survey Collaboration 2005, see also Rykoff et al. 2016), finding $>10^5$ cluster candidates in total. It differs from other commonly-available cluster catalogues, in that it is a 'bottom–up' photometric selection with the goal of searching for a red sequence, rather than applying a 'friends-of-friends' method to available spectroscopic data; a method more effectively used by spectroscopic surveys with large volumes and high completeness (e.g. Galaxies And Mass Assembly survey; Robotham et al. 2011).

As of 2015 November, the CODEX catalogue contains 6693 X-ray detections with corresponding redMaPPer targets within the largest region of the SDSS footprint (see fig. 2 of Clerc et al. 2016). The catalogue includes numerous cluster physical properties derived from X-rays or indirectly through X-ray scaling relations, including: rest-frame [0.5–2] keV band $L_{\rm X}$ measurements, cluster mass estimates, and $T_{\rm X}$ measurements (refer to Cibirka et al. 2016 for a recent use of the CODEX sample). As of 2016 August, 1633 cluster candidates from CODEX with X-ray peaks within 30 arcmin of the corresponding luminosity-weighted centroids in SPIDERS have thus far undergone observations (with 1337 having been fully completed). This sample of cluster candidates forms the basis of our BCG sample. All of the optical imaging data used here were taken from the SDSS DR12 release (Dawson et al. 2016; data are calibrated as in DR10), which includes all BOSS data from SDSS-and offers improved iiisky subtraction over previous releases (see Blanton et al. 2011; Häußler et al. 2013).

2.2 Sample selection

Initial cuts to the SPIDERS sample are outlined in Clerc et al. (2016). These include: an SDSS *i*-band magnitude cut (measured in a 2 arcsec aperture) of $17.0 \leq$ FIBER2MAG_I ≤ 21.2 to maximize the efficiency of the redshift detection algorithm and a requirement that any source must have $\geq$4 X-ray counts from *ROSAT*. These cuts are deliberately lax to retain as many candidates as possible; visual inspection efforts on the velocity distributions of cluster members are ongoing by the SPIDERS collaboration at the time of this publication in order to better characterize and identify cluster membership (see upcoming paper, Clerc et al., in preparation, see also Section 3.1).

We impose several extra cuts on the sample of 1633 cluster candidates prior to use. First, we follow the work of Stott et al. (2012) and impose a cut on the redMaPPer photometric redshift estimates of our objects as such that Z_LAMBDA ≤ 0.3, in order to ensure decent-quality optical photometry (765 objects). We then adopt a richness cut of LAMBDA_CHISQ_OPT ≥ 20 to minimize the number of objects in our sample that are not true clusters (Finoguenov, private communication; see also Rykoff et al. 2014), such as objects in close projection with wildly differing spectroscopic redshifts (see also Clerc et al. in preparation), or X-ray loud AGN affiliated to a red sequence identified by redMaPPer (470 objects). The latter detections are accommodated for in richness measurements by applying an AGN halo occupation distribution model; roughly 2 per cent of clusters at $z < 0.3$ and with richness > 30 are thought to be affected. A final cut required NHASZ ≥ 10 (i.e. more than 10 redMaPPer-determined cluster members with at least one SDSS-DR14 spectroscopic measurement spectroscopic observations), following Collins et al. (1995). This selection criterion ensured there were enough remaining members to compute robust velocity dispersion estimates, our chosen method to estimate cluster dynamical masses (see Section 3.1). After these criteria were applied, a total of 433 cluster candidates remained for visual inspection.

2.3 BCG identification

In this work, an object which we call a 'BCG' may not always be the object designated the 'brightest' magnitude in a given red sequence detected by redMaPPer. Here, we adopt the definition of a 'BCG' as being the 'brightest' galaxy in closest angular proximity to the measured X-ray centre of our clusters (e.g. Lin & Mohr 2004). This definition has led several authors to preferentially adopt the term 'central galaxy', or CEN/CG (e.g. Guo et al. 2009; Oliva-Altamirano et al. 2017 and others) to clarify their selection, for example, in the case of clusters with comparably bright, infalling galaxies. In our case, however, as we do not probe the group regime where designating a central galaxy is often much more ambiguous (e.g. Yang et al. 2005), we use the term as a synonym for the classical, high-mass galaxies which reside in cluster centres.

There are several issues which can result in incomplete cluster membership. From an instrumental standpoint, the fibres on the BOSS spectrograph have a minimum separation limit of 62 arcsec (55 arcsec for the SDSS I/II spectrograph), corresponding to a physical scale of $\sim$100 kpc at $z = 0.1$, which may exceed the projected separation between objects in dense source fields (e.g. rich clusters or regions close to the galactic plane), thereby causing incompleteness issues (e.g. von der Linden et al. 2007; Miller et al. 2005, which reported a cluster core completeness level of $\sim$50 per cent). In these cases of high source density, the fibre assignment algorithms in the SDSS may breakdown and measure objects outside of the prior targeting order (e.g. Blanton et al. 2003). With these caveats in mind, some groups opt to use integral field unit observations on clusters rather than traditional slit spectroscopy, where simultaneous observations of objects can be taken at increased source density (e.g. Karman et al. 2015). Alongside instrumental issues, the survey design, in particular the magnitude threshold of $m_{\rm i} > 17.0$, may also lead to omitting BCGs in some SPIDERS clusters from the targeting process, due to their brightness in comparison to other cluster members. There are also additional factors which can affect how redMaPPer selects red-sequence objects which it identifies as clusters. For example, the wings of bright sources (i.e. stars) may affect the photometry of fainter objects in close projection on the sky, which can lead to misclassification or omission from the colour–magnitude decision tree method used by redMaPPer. BCGs which

have colours statistically atypical with respect to other cluster members may also not be detected, such as those that have high central star formation rates and therefore significantly bluer central regions (e.g. NGC 1275, Fabian et al. 2003).

For these reasons, we deemed it necessary to visually inspect all BCG assignments and clusters by eye. At this stage, we do not make any additional effort to characterize other members than the BCG; details on the automated clipping procedure and velocity dispersion algorithms can be found in Section 3.1. As aforementioned, we acknowledge that this sample may be slightly biased against objects significantly outside of the red-sequence of their parent cluster because of redMaPPer selection criteria. However, BCGs with abnormally large central star formation rates (>100 $M_\odot$ yr^{-1}) rare with respect to the general population of BCGs at the redshift range in this work (e.g. Loubser et al. 2009; Green et al. 2016), with recent estimates on the order of 10 per cent or lower. Moreover, we believe that any omitted objects are predominantly due to fibre collision problems rather than a result of the redMaPPer algorithm, which we discuss below.

The *gri* composite fields were predominantly used to visually inspect the cluster candidates (inspection carried out primarily by K. Furnell). During inspection, member coordinates were extracted from the SPIDERS catalogues and displayed on the images, along with the X-ray centroid, in order to check the robustness of the assignments. We followed a similar selection prescription to Stott et al. (2012), where we select the brightest galaxy at the tip of the red sequence within R_{200} of the X-ray centroid (see Finoguenov et al., in preparation). As well as being the most robust identifier of BCGs (e.g. Lin & Mohr 2004), this definition was also found by George et al. (2012) to be the best observational proxy for the centre of clusters in general. The R_{200} used here were taken from the CODEX estimates from X-rays.

In $\sim$20 per cent of clusters, the true BCG was either incorrect or missing from the SPIDERS catalogues. There were occasional cases where the likelihood ranking of an object being the BCG was incorrectly stated in the catalogue, with the BCG candidate which met our selection criteria ranked lower in the listing (12/433 candidates). More often, however, the BCG listed in the catalogues tended to have been omitted during the SPIDERS selection process (86/433). In these cases, the most visually likely BCG candidate was extracted via sextractor and cross-matched with all of the spectroscopy available up to DR14 within 5 arcsec (over 4 million objects in total). Only 29 per cent (25/86) of BCGs were recovered in this way ($\sim$5 per cent of the selected sample after cuts). We therefore argue that most omissions are due to fibre collision issues, as there is no spectroscopy for these objects across the SDSS available despite a red sequence identified by redMaPPer. This value is in line with Rykoff et al. (2014), which quotes an estimate of misidentified centrals at the 5 per cent level. Recent efforts have gone into quantifying the ability of the redMaPPer algorithm to correctly centre clusters, with similar results (Hikage et al. 2017). A summary of the various cuts applied to form the sample are shown in Table 1.

In total, 329/433 objects passed the visual inspection stage and cuts. A number of example BCGs can be seen in Fig.1; all of them have early-type morphologies. In this analysis, we opted to reject BCGs with obvious tidal features from undergoing a major merger (7/104) as well as ones with obvious image issues, such as exceptionally bright stars, extensive field overcrowding (e.g. for a few fields close to the galactic plane (none of the sample however lie within $-25^\circ \geq b \leq +25^\circ$) and object truncation due to proximity to field edges (22/104). The remainder were either algorithm

Table 1. Summary of the BCG selection. The bold values represent the initial sample after quality cuts, the number of objects omitted after visual inspection and the total number of BCGs in the final sample respectively.

Description	Number
CODEX-SPIDERS 30 arcsec match	1633
+ Z_LAMBDA $\leq$ 0.3	765
+ LAMBDA_CHISQ_OPT $\geq$ 20	470
+ NHASZ $\geq$ 10	**433**
Omitted	**104**
a) Image issues	36
b) Missing	61
c) Major merger	7
BCG candidates (including legacy SDSS)	**329**

'artefacts' (such as a wrongly attributed CODEX X-ray source to a red sequence detected by redMaPPer, or a projected overdensity of objects with similar photo-z values from redMaPPer but highly variable spec-z values; 14/104) or had no spectroscopic redshift available in the legacy SDSS archive within a 3 arcsec match (61/104).

3 ANALYSIS

3.1 Cluster properties

Three independently measured cluster properties are used to characterize the clusters in our sample: halo mass M_{200} (with respect to the critical density), X-ray luminosity L_X, and cluster richness λ, the latter two of which we take directly from the SPIDERS catalogues. The richness values we use originate from redMaPPer and represent the summed *probability* of galaxy membership for a given cluster with redshift taken into account, shown by Rykoff et al. (2012) to be a superior measure of total membership than imposing a basic colour cut criterion. In addition, the L_X values represent the total aperture-corrected luminosity across the entire [0.5–2] keV band (see Finoguenov et al. 2007 for the correction method). The corresponding $L_X - z_{RM}$ distribution for our clusters is shown in Fig. 2. We limit our clusters at the analysis stage to those above 10^{43} erg s^{-1}. This was done primarily because such objects constitute poor clusters and low-mass groups, often with less well-constrained X-ray measurements in the context of RASS data (e.g. Böhringer et al. 2001). If included, however, we observe very little change to our results (less than 5 per cent in most cases).

In this work, we rely on velocity dispersion as a proxy for dynamical cluster mass. The velocity dispersion of a cluster is known to be an effective tracer of the overall mass of the cluster halo (e.g. Caldwell et al. 2016), however, this technique is prone to certain biases. For example, in the case of colliding clusters, atypically high galaxy peculiar velocities can also arise due to the cluster being out of dynamical relaxation (as an example, the Bullet cluster has a velocity dispersion of $\sim$1500 km s^{-1}, see Markevitch et al. 2002). In addition, interlopers along the line of sight can cause significant problems if not accounted for correctly, which is often a non-trivial task (e.g. Miller et al. 2005). In the context of recent studies, Maughan et al. (2016) found that cluster masses derived from velocity-based caustics were biased high by $\sim$ 20 per cent. Although their caustic-based method differs from that used here, their work represents a useful indication as to how much of a deviation one should expect using velocity-based mass proxies.

We use a similar prescription in this work to that of Clerc et al. (2016) when computing the velocity dispersions of our clusters. We

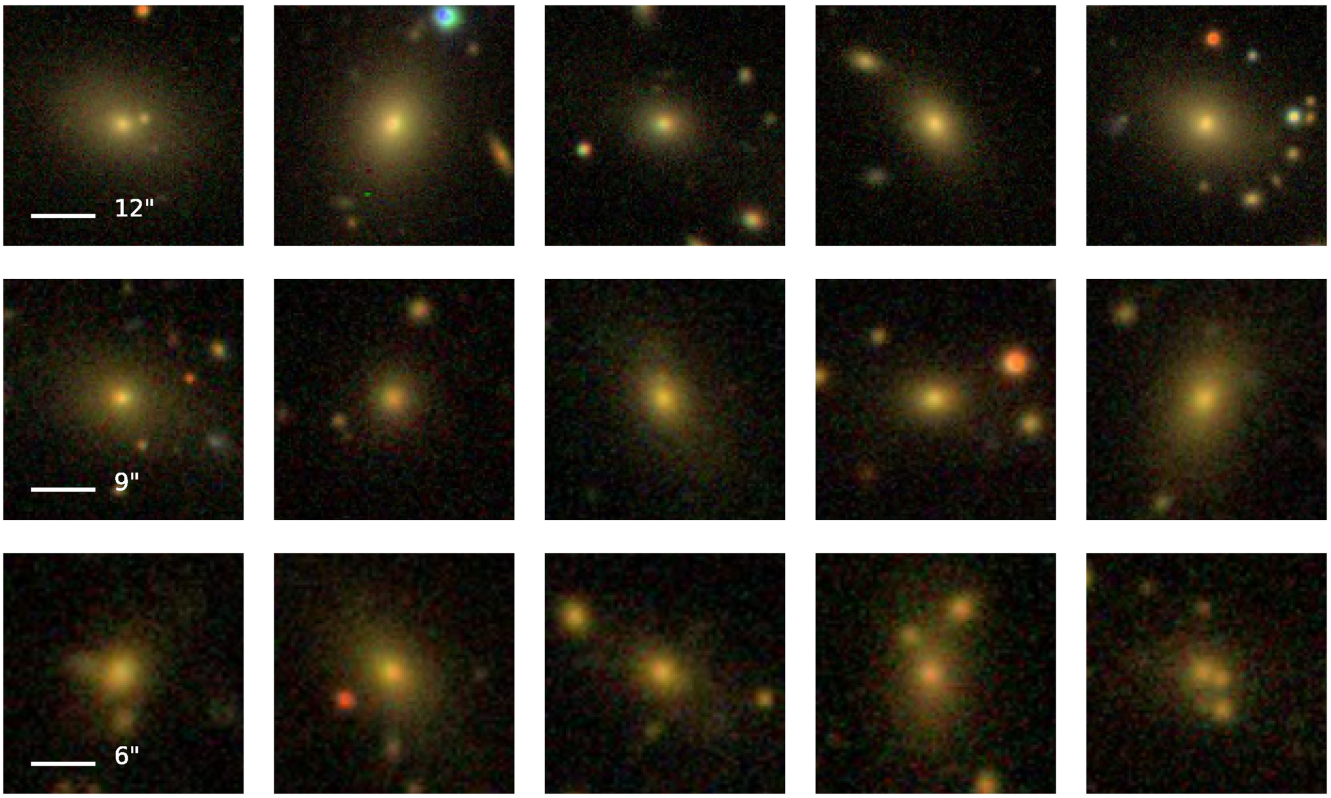

Figure 1. Example false-colour SDSS *gri* composites of 15 BCGs used in this study (100 × 100 kpc for each tile). Each of the three horizontal panels represents a sample of five randomly drawn BCGs about the 16th, 50th, and 84th redshift percentiles from left to right (0.1, 0.18 and 0.25, respectively). The white line represents an equivalent scale of ∼25 kpc (angular equivalent rounded to the nearest arcsecond).

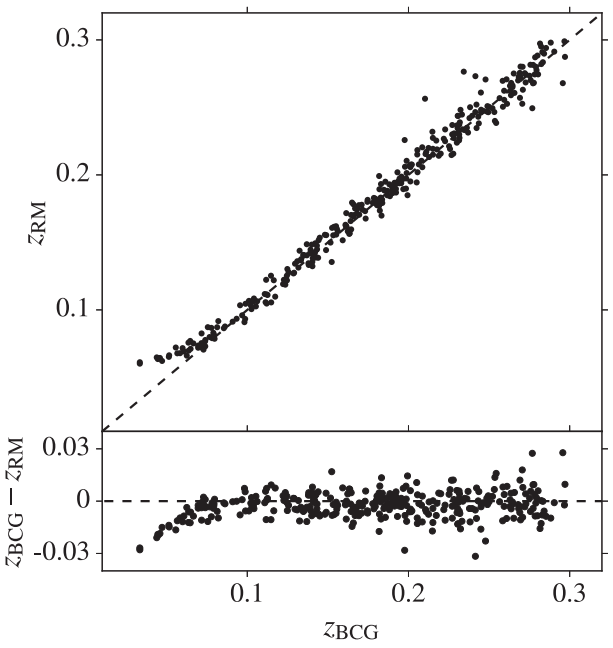

Figure 2. L_X–z_{RM} distribution for the clusters in our sample. The black circles show the initial 329 clusters which passed our visual inspection, whereas the red points represent the 198 BCGs used in our final analysis (see Section3.4).

make no prior assumptions about the membership of objects contained in the SPIDERS catalogues, requiring only that they meet our quality cuts (see Section 2.2). We do, however, apply an additional cut before computing our velocity dispersion estimates to remove projected interlopers, in that we require a galaxy to lie within a projected distance of $R \leq 2 \times R_{200}$ from the designated BCG.

For a given cluster member, we follow the standard practice of computing its velocity with respect to the cluster rest frame (e.g. Carlberg et al. 1996):

$$\frac{v_i}{c} = \frac{z_i - z_{clus}}{1 + z_{clus}}, \quad (1)$$

where v_i is the recession velocity of a member galaxy, z_i is its corresponding redshift value, and z_{clus} is the redshift of the cluster. We applied an iterative clip to our cluster redshift values in velocity space, imposing a $\pm 3000\,km\,s^{-1}$ threshold about the median velocity of the cliplist, which was recalculated at each step. We then estimated the final cluster redshift using a biweight.

We apply the same cut in velocity space to our object list, requiring again that a given galaxy be within $\pm 3000\,km\,s^{-1}$ with respect to the median cluster velocity; galaxies outside this limit were flagged as interlopers and discarded. The final object list underwent an iterative 3σ clip, which was allowed to run until convergence. Clipped object lists with $N < 10$ members were rejected, and a mass was not computed for the cluster (e.g. Collins et al. 1995).

Following the methodology outlined in Beers, Flynn & Gebhardt (1990), we use two different measures of velocity dispersion, dependent on the number of remaining cluster members. For $10 < N \leq 15$, we apply the 'gapper' method, which is optimized for clusters with a low member count (see Beers et al. 1990). For a list of mem-

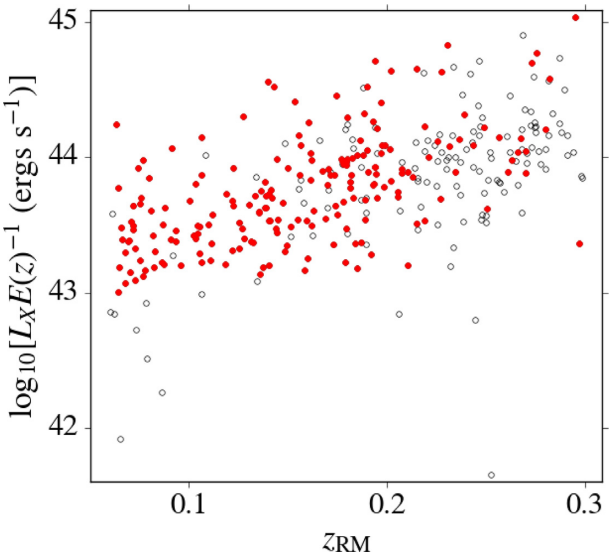

Figure 3. Spectroscopic redshift of the visually inspected BCGs (z_{BCG}) versus photometric cluster redshift (z_{RM}) comparison for the sample of 329 objects (typical errors are $\Delta z_{BCG} \sim 10^{-5}$ and $\Delta z_{\lambda} \sim 0.01$, respectively). The black dashed line is the 1:1 relation. In general, the BCG redshifts agree well with the cluster photometric values, albeit with some scatter at higher z (see Section 3.1). The discrepancies in photometric redshift at $z \leq 0.08$ are discussed in detail in Rykoff et al. (2014).

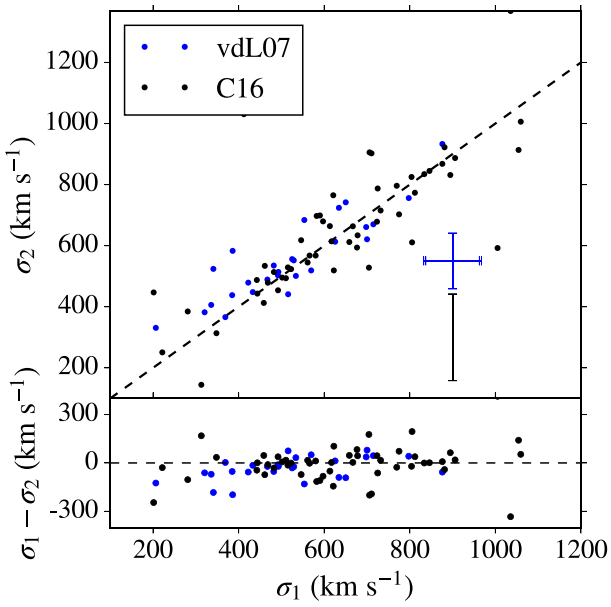

Figure 4. Comparison plot between 81 velocity dispersion values computed here (y-axis) and those computed by von der Linden et al. (2007) and by Clerc et al. (2016) for 27 and 54 common clusters respectively, accounting for duplicates (x-axis). The average 1σ error for each of the two samples are plotted in the bottom right hand corner.

ber galaxy line-of-sight velocities in ranked order, one can use the 'gaps' between them to achieve a sense of scale for the underlying distribution:

$$\sigma_{200} = \frac{\sqrt{\pi}}{n(n-1)} \sum_{i=1}^{n-1} w_i g_i, \tag{2}$$

where σ_{200} is the velocity dispersion and n is the variable rank. The 'gaps', g_i, are defined as:

$$g_i = v_{i+1} - v_i\,, \tag{3}$$

for $1 \leq i < n-1$, where v_i is the velocity of a galaxy ranked at i. These gaps are then 'weighted' with rank-dependent weights w_i:

$$w_i = i(n-i)\,. \tag{4}$$

For clusters with a larger number of remaining members ($N > 15$), we adopt a biweight technique as it generally represents a more robust statistic. In both cases, errors on our velocity dispersions are estimated from 68 per cent confidence limits taken from 10 000 bootstrap realizations, with the mean error $\Delta\sigma_{200} \sim 20$ per cent.

For mass estimates, this work follows Finn et al. (2005), who adopt the following equation for cluster mass:

$$M_{200} = 1.2 \times 10^{15} \left(\frac{\sigma_{200}}{1000 \text{ km s}^{-1}}\right)^3 \times \frac{1}{\sqrt{\Omega_\Lambda + \Omega_M (1+z)^3}} \, h_{100}^{-1} M_\odot. \tag{5}$$

Of the clusters used in this work, 318 have measured velocity dispersions and thereby corresponding dynamical mass estimates. The clusters themselves span a large range of masses, from $10^{13} \leq M_{200} \leq 10^{15} (M_\odot)$ (median $= 1.4 \times 10^{14}\,M_\odot$; see Section 4). It was found at this stage that a further two BCGs had large deviations in redshift from their corresponding z_{clus} (SPIDERS ID 1_6003 and 1_21735, see Fig. 3); these clusters were flagged and did not factor into any further analysis. For reference, we present a comparison between σ_{200} estimates for an overlapping sample of 27 and 54 SPIDERS clusters with von der Linden et al. (2007) and Clerc et al. (2016), respectively, in Fig. 4. In an upcoming paper to be released by the SPIDERS collaboration, we attempt to address these issues through visual screening efforts with the aim of retrieving more accurate estimates of velocity dispersion (Clerc et al. in preparation; see Clerc et al. 2016 for method).

3.2 BCG structural parameters: the Sérsic profile

In order to gain information about the morphological properties of our BCGs, we model their light profiles in two dimensions (see Stott et al. 2011 for an example in the context of BCGs). The image data used in this work originate from the SDSS DR12 release (Alam et al. 2015). The data have been scaled, preprocessed and have undergone a global background subtraction following Blanton et al. (2011). The background treatment is much improved over the sigma-clipping method used in releases prior to DR8 (see fig. 12 from Blanton et al. 2011 for comparison), which is known to oversubtract the profile wings of high-Sérsic index objects such as BCGs (e.g. Bernardi et al. 2007). Here, we choose to use these estimates for the global sky during fitting, which we discuss in Section 3.3.

The BCGs in this work are modelled by a single-Sérsic profile (Sérsic 1963), which has the form

$$I(R) = I_e \exp\{b_n[(R/R_e)^{1/n} - 1]\}, \tag{6}$$

where $I(R)$ is the surface brightness of an object at radius R, R_e is the effective radius within which 50 per cent of the object light is contained, I_e is the object surface brightness at the effective radius, n is the Sérsic index, and b_n is a product of incomplete gamma functions as described in Ciotti (1991). The empirical Sérsic profile is a good description of the light distribution of BCGs, which are predominantly bulge-dominated and ellipsoidal in nature (see Graham & Driver 2005 and references therein). The integrated magnitudes

produced from Sérsic fitting have the additional advantage that they account for more light than traditional Kron/Petrosian magnitudes for objects with high-n, the latter of which can underestimate the true brightness by as much as 95 per cent (Graham & Driver 2005).

For the purposes of this study, we opt to fit a single-Sérsic component to each BCG. There is some debate in the literature as to the most appropriate number of Sérsic components which should be fit to a galaxy in order to accurately estimate galaxy parameters. For example, Bernardi et al. (2014) experimented with fitting single- and double-Sérsic fits to a series of simulated single- and double-Sérsic galaxy images. They found that both the single- and double-Sérsic fits perform well at the bright end ($M_r > -21$) regardless of galaxy type, with both models increasingly ill-suited to their opposing galaxy type at fainter magnitudes. It was shown that a single-Sérsic fit to what is, in reality, a double-Sérsic galaxy is as inappropriate a model as applying a double-Sérsic fit to what is, in reality, a single-Sérsic galaxy. On closer inspection of the light profiles for most of our BCGs, we found no significant evidence for the addition of a secondary component, so therefore adopt a single Sérsic as our model type to fit to each BCG.

Numerous profile-fitting codes exist in the literature, such as: GIM2D (Simard 1998), PROFIT (Robotham et al. 2017), IMFIT (Erwin 2015), PYMORPH (Vikram et al. 2010), and GALFIT (GALFIT3, Peng et al. 2010). For this work, we opt to use GALFIT, which uses a Levenberg–Marquardt ('downhill-rolling') based χ^2 minimization technique for fitting light profiles (see Kennedy et al. 2016 for a recent use of the software). It is also capable of generating light profiles based on fixed input parameters, which we use to create mock galaxies as described in Section 3.4.

We run GALFIT using the Structural Investigation of Galaxies via Model Analysis code, or SIGMA (Kelvin et al. 2012), which is an R-based pipeline software used with great success in the GAMA survey (Driver et al. 2011) to provide Sérsic model fits to 167 600 galaxies in five optical (SDSS–*ugriz*, Fukugita et al. 1996) and four near-infrared (NIR, UKIRT–*YJHK*) passbands (see Hill et al. 2011). SIGMA is capable of performing a full fit, including: object extraction through SOURCE EXTRACTOR (SEXTRACTOR; Bertin & Arnouts 1996), creating a model of the field point spread function (PSF), estimating the local sky about an object, masking external objects and, finally, fitting a profile through GALFIT. Details of our implementation of SIGMA are provided in the upcoming section; more specific information can be found in Kelvin et al. (2012).

3.3 SIGMA pipeline and implementation

SIGMA is designed to fit objects in multiple bands in tandem, requiring only the coordinates at which an object is located as an input file alongside any image data corresponding to the desired fitting bands. SIGMA produces an output file containing any relevant SEXTRACTOR parameters used in fitting, the background estimate (if requested), and the profile-fitting results from GALFIT. A description of the pipeline is given below, alongside any parameter settings used here when running SIGMA.

(i) *Image cut-out*: To begin, accesses the WCS information in the header of an image file containing an object. It then converts the celestial R.A./Dec. coordinates of an object into *x*/*y* Cartesian pixel coordinates using the SKY2XY routine in the WCSTOOLS package (Mink 1998). The upper and lower limits of a 1201×1201 pixel region centred on the primary object are determined. This cut-out, designated the 'primary science image' is used during analysis from this point forward.

(ii) *Source extraction*: then runs SEXTRACTOR on the primary science image to detect any objects in the field. During extraction, we applied the default parameters: DETECT_THRESH $= 2\sigma$, DETECT_MINAREA $= 10$, and SATUR_LEVEL $= 25\,000$. The image is also filtered through a 5×5 pixel Gaussian convolution kernel with full width at half-maximum (FWHM) $= 2$ pixels prior to detection; SEXTRACTOR defaults are used everywhere else. Outputs from SEXTRACTOR corresponding to the primary object provide initial parameter estimates for the algorithm. Any extra object detections about the primary object are designated 'secondary' sources. The number of secondaries to be used during fitting is specified by the user prior to running ; any other objects are designated as 'tertiaries' and masked out prior to fitting (see vi).

(iii) *PSF extraction*: the output catalogue from SEXTRACTOR is used to find objects in order to estimate the PSF of the field. The PSF EXTRACTOR software package (PSFEX; Bertin 2013) is applied to create the empirical PSFs used in , which are smoothed by fitting the end result with a Moffat profile (Moffat 1969). For an object to qualify for computing the PSF, requires an S/N > 10 and an eccentricity, ϵ, of >0.05. PSFEX then estimates the FWHM of the object, requiring that $2 <$ FWHM < 10 pixels and that the object lies within the central 50 per cent of the distribution. A minimum of 10 objects are required to compute a PSF; if this criterion is not met, will loop back and attempt to run PSFEX on a larger cut-out area. Upon completion, the final result is a 25×25 pixel PSF estimate, which is used in fitting with .

(iv) *Sky subtraction*: to estimate the local sky about an object, uses an adaptive mesh technique dependent on the size of the primary object (see section 3.3 of Kelvin et al. 2012). Within each 'cell' of the mesh, computes the median background level and fits a smooth spline across the frame, subtracting the background estimate from the science image. Although suitable for objects in the field/groups, we prefer not to apply any additional background subtraction to our images due to the nature of the cluster environment. In the cores of clusters, it is often the case that galaxies have overlapping profile wings. In addition, cluster cores also have a faint intracluster light (ICL) component, thought to have formed primarily from stars ejected from galaxies through mergers, tidal stripping, and harassment (Gonzalez, Zaritsky & Zabludoff 2007; Mihos et al. 2005; Burke et al. 2012). Therefore, we opt to use the global SDSS estimates when fitting our objects to avoid any sky bias at local scales, primarily as it is known that sky overestimation has a significant impact on the final fit of an object (e.g. Graham & Driver 2005). We explore the impact of field-by-field variations on object fitting in our simulations (Section 3.4).

(v) *Object masking*: produces segmentation maps that can be used as object masks; the mask shape and the number of sources to be used during fitting are specified by the user. In this work, we apply inner (to minimize the effect of PSF-sensitive cores on our fits), outer, and tertiary masking to our objects, using a pixel buffer of 5 and a 1 pixel mask to the inner region. We impose a maximum limit of three unmasked secondary sources within 2.5 mag of the primary source; we choose this value primarily as a compromise between computational efficiency and resolving parameter degeneracies at the fitting stage.

(vi) *Profile fitting*: Prior to fitting, creates a further cut-out of the science image based on output parameters from SEXTRACTOR for the primary object. As aforementioned, initial guesses for both the primary object and secondary objects are taken from SEXTRACTOR, including: object magnitude, axis ratio, position angle, and effective radius R_e (see Kelvin et al. 2012 for details of the effective radius estimation). The initial estimate of the Sérsic index n is set to a constant value of 2.0; however, changing this value was found by

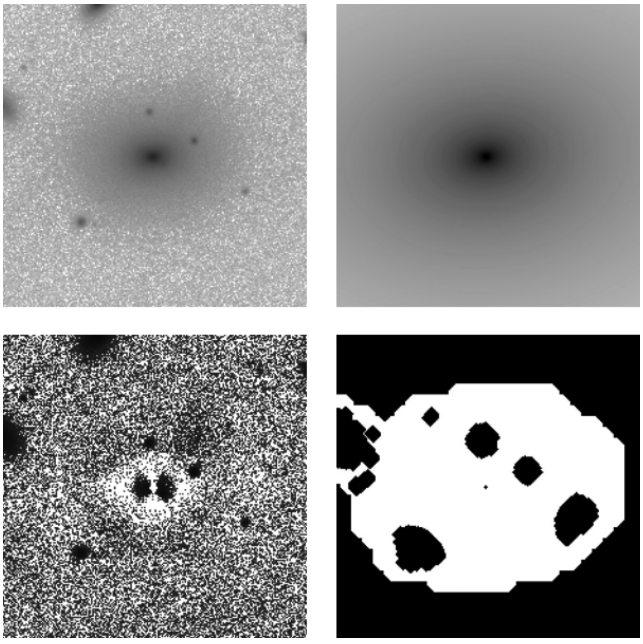

Figure 5. An example data product from for the BCG in cluster 1_1365 (100 × 100 kpc, $z \sim 0.05$). Clockwise from top left: SDSS *r*-band image, Sérsic model from , image mask, residual (enhanced to bring out faint artefacts). Except for the binary mask, all other quadrants are scaled logarithmically.

Kelvin et al. (2012) to have little effect on the final result. We modelled our objects with a free Sérsic profile ($1 < n < 20$), imposing no manual constraints beforehand on any output parameters (see discussion below).

In order to impose quality control on the GALFIT output values, SIGMA contains inbuilt constraints which are then applied post-fitting. After running GALFIT on an object, SIGMA analyses the output and refits any objects which are flagged as follows:

(i) GALFIT has encountered a serious error that prohibits completion of the fit.
(ii) The primary object's centre has undergone a migration of $x^2 + y^2 > R_{\rm e,\,initial}$.
(iii) The primary object's end radius is either exceptionally large ($\log_{10}(\frac{R_{\rm e,final}}{R_{\rm e,initial}}) > 3$) or exceptionally small ($\log_{10}(\frac{R_{\rm e,final}}{R_{\rm e,initial}}) < -3$).
(iv) The primary object's end ellipticity is high ($\epsilon > 0.95$).

In total, 326/327 objects were fit with profiles from SIGMA; we discuss the use of the *i*-band model profiles when computing stellar masses in Section 4.1 and our choice of the *r* band for the morphological parameters. Of these, 198 galaxies were used in our subsequent analysis, which we discuss in the upcoming section. An example of the finished SIGMA data product for a BCG is shown in Fig. 5.

3.4 Probing surface-brightness limits with simulated profiles

As our BCGs encompass a large magnitude range, we decided to investigate any potential structural dependencies that may arise with changes in surface brightness or $R_{\rm e}/n$. Little investigation has been done to understand such biases which arise a result upon fitting (see Guo et al. 2009; Blanton et al. 2011; van der Burg et al. 2017 as examples of studies that attempt to characterize structural biases), with numerous authors content to base their fit quality on the reduced χ^2 estimate ($\chi_\nu{}^2$). These fits are not necessarily representative of a result which is physically meaningful (e.g. Liu et al. 2008 found differing results for their BCGs, dependent on the isophotal level chosen or method of background subtraction). Some studies have even adopted a novel approach to their fitting in order to gain insight into the 'goodness of fit' of their objects; a recent example being Lange et al. (2016), who fit their objects with SIGMA using a Monte Carlo-based method, taking the resulting parameters for each fit at the point of convergence.

Table 2. Cluster fields used when inserting mock galaxies. The ID column refers to the corresponding ID string in the SPIDERS catalogues.

ID	α_{2000}	δ_{2000}	RUN	CAMCOL	FIELD
1_1282	133.761	+55.454	1350	2	194
1_14572	352.634	+20.728	8096	6	182
1_2785	143.215	+47.931	2740	6	261
1_2952	163.487	+49.499	2883	1	109
1_3349	202.598	+49.185	3650	5	85
1_4285	146.506	+43.127	2887	4	251
2_11151	11.534	+20.614	7913	5	30
2_2401	126.401	+48.341	1331	4	156

We therefore tested SIGMA's ability to recover parameters from BCG-like objects with the fitting criteria specified in Section 3.2 by creating a grid of model profiles with known input parameters, which we then inject into real SDSS fields. The eight SDSS fields selected for use in the simulations are listed in Table 2. Although they were taken from among the fields in the sample, the selection process was effectively at random. The fields contain many features known for causing issues during fitting, such as bright stars and regions of high source density.

The model profiles were generated using GALFIT for consistency, as it was the algorithm of choice used during fitting. The estimated magnitude zero-points and PSFs (from SIGMA) for these fields were used when generating the model profiles, to account for field-by-field photometric variations. An idealized Poisson noise component was also added, to mimic shot noise. The models were then injected into each of the eight fields at eight random, fixed positions, and subjected to a full run through the SIGMA pipeline. We chose a range of Sérsic indices from 1 to 10 in steps of 1, apparent magnitude values from 12 to 19 in all three bands, and effective radii from 10 to 100 kpc at z= 0.2 (equivalent to 0.253 arcsec kpc^{-1}). Therefore, a total of 6400 model combinations per band were created, or 19 200 in total. We chose this scale for $R_{\rm e}$ as it represents the approximate peak of the SPIDERS sample, so will correspond to effective radii relevant for our purposes. In addition, we justify our selection of input Sérsic indices by noting that they encompass the bulk of all potentially physically meaningful outputs; Sérsic indices larger than $n = 10$ represent virtually identical profiles (e.g. Graham & Driver 2005). Finally, the input axis ratio was held constant at 0.66 (a realistic value for most BCGs; most SPIDERS BCGs have axis ratios between 0.6 and 0.8 with little variation across bands) and the position angle at 50° (not significant in the context of this study); this was primarily done for the sake of preserving computational resources, so to reduce the number of potential parameter combinations to simulate.

We refer the reader to Appendix A for the simulation results in the *g* and *i* bands, as we choose to use the *r*-band profile parameters for our BCGs. The full outputs for the *r*-band run are shown in Fig. 7, for which we note several initial observations. First, that there is an obvious co-dependency between n and $R_{\rm e}$; the outputs are affected

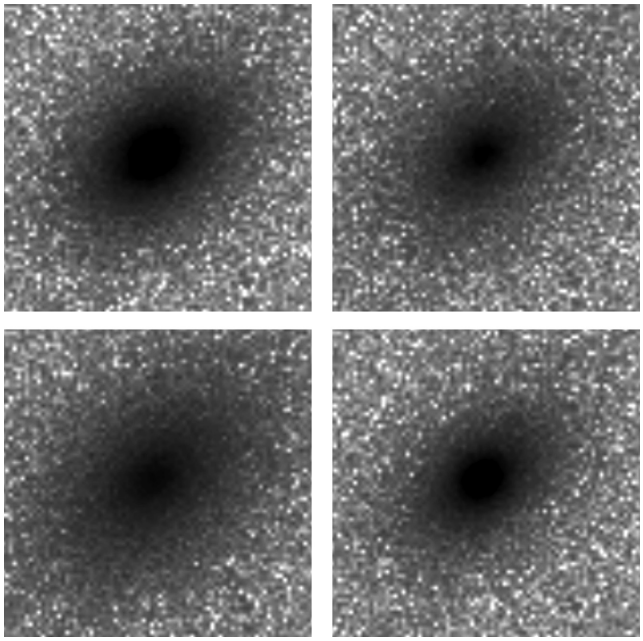

Figure 6. Example *r*-band simulated profiles at 15th magnitude (tiles scaled to 100 × 100 kpc with an assumed redshift of 0.2). Top: for a fixed n of 4, $R_e = 20$ and 80 kpc. Bottom: for a fixed R_e of 40 kpc, $n = 2$ and 8. Note the change in surface-brightness distribution in either case.

if either is changed (e.g. Graham et al. 1996). Brighter than 17th magnitude, the effect is minimal, with an average scatter about the input of ∼5 per cent in Sérsic index for a given stepwise change in effective radius and ∼20 per cent vice versa in effective radius for each incremental change in Sérsic index. In general, magnitude values are accurately recovered; we see an average scatter of ∼0.1 mag about the input value, regardless of whether n or R_e is changed. As is visible however, the scatter in the values of n and R_e becomes more significant at fainter magnitudes (note the bottom two panels of Fig. 7), with the output scatter well in excess of 50 per cent at 19th magnitude.

The behaviour of the $n = 1$ profile with R_e is significantly different than for profiles where $n > 1$. At increasing effective radii, it appears that fits to the profile become 'chaotic' at ∼14th magnitude, with the scatter exceeding 50 per cent at ∼14th magnitude or fainter. Such a profile is exponential by definition and is often used as a model for disc galaxies (e.g. Freeman 1970); indeed, it is the default model in the SDSS (e.g. Blanton et al. 2011). The difficulty in fitting such extended, exponential profiles may arise from issues with additional source blending, due to the fact that $n = 1$ profiles are not strongly centrally concentrated (e.g. Fig. 6 shows the effect of changing the Sérsic index). However, this profile is generally not appropriate for galaxies such as BCGs, the majority of which are bulge-dominated and follow a de Vaucouleurs-like profile (e.g. de Vaucouleurs 1948) where $n \sim 4$ (e.g. Stott et al. 2011). Some studies have modelled cD-type BCGs with a bulge+exponential component, in order to account for their extended stellar halo which is degenerate with the intracluster light (e.g. Zhao, Aragón-Salamanca & Conselice 2015a, Donzelli, Muriel & Madrid 2011).

From our simulations, we are also able to characterize several important biases, which may have significant consequences if one were to use SDSS data when profile fitting, or when visually classifying morphologies. There is an obvious bias in Sérsic index with increasing magnitude. At ≥17th magnitude, there is a downturn in output Sérsic index with increasing effective radius (second panel from the left, Fig. 7), with the reverse being true for effective radius. We strongly suspect this result is due to a surface-brightness effect; as the wings of an object become faint with respect to the background level, they become more difficult to detect (surface brightness is dependent on both Sérsic index and effective radius). Therefore, GALFIT underestimates the true slope of the light profile. A similar effect was also reported in Vika et al. (2013) for a sample of >3000 galaxies modelled with artificially redshifted SDSS photometry. This effect is consistent regardless of Sérsic index, with all of the output values (bar $n = 1$) showing a similar reduction from input as a trend with effective radius. The effect is also independent of filter; all three bands used for fitting showed a similar bias, albeit to varying degrees of severity (see Figs A1 and A2 in Appendix A, plus discussion below).

Figs A1 and A2, also reveal a marked decrease in fit robustness moving from the g to the i band, with the scatter in output values increasing with wavelength. This behaviour is also seen in the decreasing success rates of our simulations (with 'success' defined as a given combination of fit parameters being modelled by SIGMA to completion), as presented in Fig. 8. The sky tends to be brighter at redder wavelengths (see Stoughton et al. 2002), which is reflected in the smaller magnitude limit of the SDSS i band (21.3 mag, as opposed to 22.2 for g/r). The increased sky brightness in the i band therefore significantly affects the final fit. We are therefore justified in our selection of the r-band models to characterize our BCGs, as a compromise between both band depth and the amount of k-correction necessary (Section 4.1).

For these reasons, we decided to impose a cut on the raw output magnitudes for the SPIDERS BCGs, to minimize potential biases in Sérsic index that may arise as a result of surface-brightness dimming effects. As we are unsure at the resolution of our simulations precisely where this effect begins to dominate our fits, we select a magnitude of $m_r = 16.5$ as the faintest magnitude for which to include objects. To place this choice into context with the output magnitudes from SIGMA of the BCGs in our sample, the raw output magnitude distributions are displayed in Fig. 9. The sample peaks at $m_r = 15.8$ (with $m_g = 16.9$ and $m_i = 15.2$), with ∼1/3 of all galaxies lying above the our limiting magnitude of 16.5 (99/326). Thus, the total number of objects for which we include in our analysis to 227 (198 after imposing further quality cuts as described in Section4).

Applying this cut in BCG magnitude at $m_r = 16.5$ significantly affects the redshift distribution of our clusters (Fig. 2), in that it reduces the number of intermediate-redshift clusters in the sample (notably, between $0.2 < z < 0.3$; this is also revealed by a KS test ($\log_{10}[p_{KS}] = -4.56$). However, we detect no evidence for any differences in the distributions of L_X, M_{200}, and λ between the full and magnitude-restricted samples beyond the 1.3σ level ($\log_{10}[p_{KS}] = -0.772$, -0.491, and -0.077, respectively).

4 RESULTS

4.1 Stellar masses and structural parameters

In order to ensure the quality of our fits, we set several criteria which a fit must meet in order to be included in our analysis (see Powell et al. 2017; Zhao et al. 2015a). These criteria include: a cut of $\chi_\nu^2 \geq 3$ to remove any BCGs with bad residuals, a cut of $R_e \geq 800$ arcsec, $\Delta R_e/R_e \geq 0.8$ (where ΔR_e is the statistical error in R_e from GALFIT, see Simmons & Urry 2008) and finally, $n \geq 14$. These parameters remove most fits deemed to be physically unrealistic; in total, approximately ∼9 per cent of objects were affected. Including

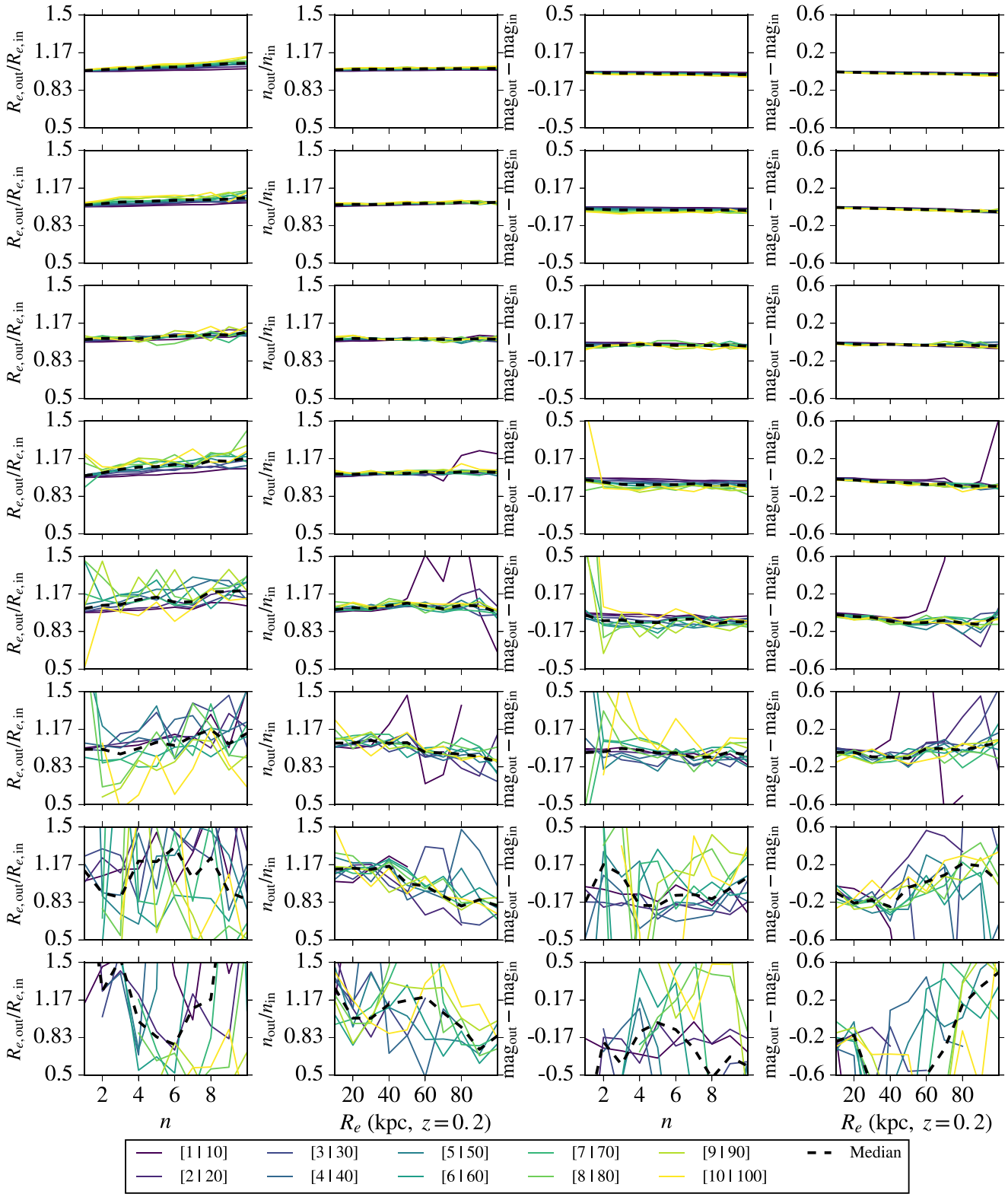

Figure 7. The results of fitting simulated profiles with in the *r* band. Each of the four horizontal panels represents the output for one of the eight fixed input magnitudes (12–19, descending). The coloured lines represent the biweighted average across the runs (assuming at least 3/8 models at each point were successfully fit; corresponding legend key [n | R_{e}] for a given colour, interchange for the relevant panel). The black dashed line represents the median [n | R_{e}] of the coloured lines. There is a clear decline in output-to-input Sérsic index with effective radius at 17th–19th magnitude (second column).

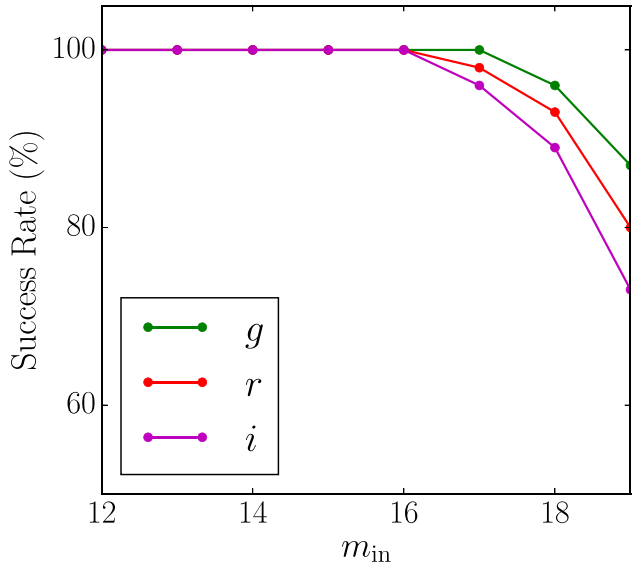

Figure 8. The fitting success rates from fitting of mock profiles. 's performance clearly degrades with both wavelength and input magnitude.

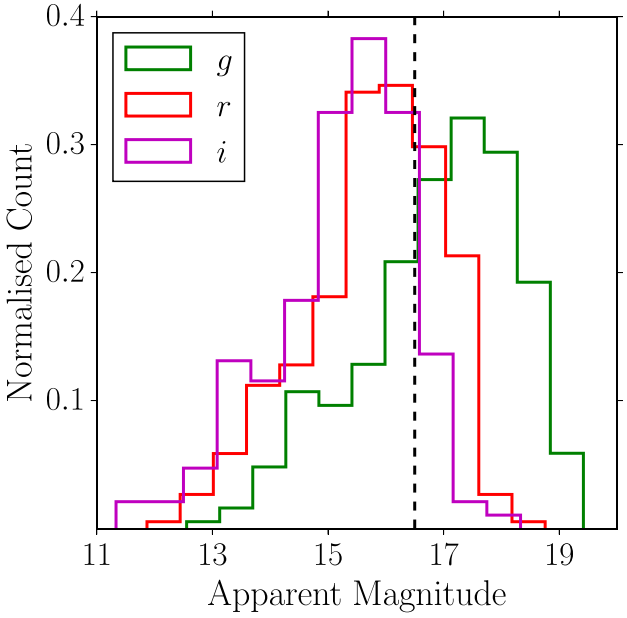

Figure 9. The raw-fit magnitudes for the SPIDERS sample from (N = 326), prior to any *k*-correction or dust correction. The histograms have been normalized by area.

the prior cuts on environmental parameters described in Section 3 brings the total number of BCGs included in our primary analysis sample to 198. We have checked and found no significant changes to our conclusions by including the fits which did not meet the stated criteria; for the sake of only adding additional statistical noise, we decided to omit them.

As the Sérsic fits to our objects produce integrated magnitudes, they can be used as a proxy for stellar mass. In this work, we adopt the updated scaling relation of Taylor et al. (2011), which was used to estimate stellar masses for galaxies in the GAMA survey. They demonstrate that stellar masses can be estimated within ∼0.1 dex of the mass estimates quoted in the MPA–JHU catalogues (195 objects, see methods in Brinchmann et al. 2004; Kauffmann et al. 2003; Tremonti et al. 2004). Taylor et al. (2011) also reported that using the *i* band as a tracer of galaxy mass produced results of similar quality to using the common proxy of NIR flux. The scaling relation is derived from spectral energy distribution (SED) fits to GAMA galaxies using SDSS *ugriz* photometry, using stellar population synthesis models from the library of Bruzual & Charlot (2003) with a Chabrier (2003) initial mass function (IMF).

From the rest-frame $g-i$ colour of a galaxy and its absolute magnitude $M_{\rm i}$, the stellar mass is estimated via the following empirical relation:

$$\log_{10}[M/{\rm M}_{\odot}] = 1.15 + 0.70(g-i) - 0.4M_{\rm i}\,, \quad (7)$$

where $M_{\rm i}$ are the *k*-/dust-corrected absolute magnitude values in the *i* band, derived from the best-fitting Sérsic profile for a given BCG and $g-i$ is its rest-frame colour. We measure the $g-i$ colours of our objects through fixed 30 kpc apertures, which we do to reduce potential biases which may occur across fits (see Section 3.4).

We correct our objects for extinction from Galactic dust using the standard maps of Schlegel, Finkbeiner & Davis (1998) (updated normalization in Schlafly & Finkbeiner 2011), with a Fitzpatrick (1999) reddening law. Typically, this correction is small; the mean values in each band are 0.08, 0.06 and 0.04 mag in *g*, *r*, and *i*, respectively. We also apply a *k*-correction to our objects after correcting for dust. The *k*-corrections are based on the work of Chilingarian, Melchior & Zolotukhin (2010) and work well for galaxies up to z ∼0.5 in lieu of multiband photometry. They are approximated by polynomials (e.g. Collins & Mann 1998), requiring only a redshift and input colour. We use our aperture $g-r$ colours; the average *k*-corrections are 0.59, 0.19, and 0.10 mag in *g*, *r*, and *i*, respectively.

We caution the reader that our mass 'errors' are drawn from the systematic errors output by the best-fitting model from GALFIT; they are therefore likely to be underestimated. Instead, we offer a comparison between the stellar masses of our final sample of objects between a common subsample of 192 with valid masses drawn from the MPA–JHU value-added catalogue in Fig. 10 (Bruzual & Charlot 2003, SP; Kroupa 2001, IMF). The agreement is good, with the average scatter (approximately ±0.06 dex) similar to that predicted by Taylor et al. (2011). The small, positive offset is predominantly due to our choice of using model magnitude when computing our stellar masses, so as to account for additional mass in the wings of our BCGs. The BCGs span a large range in mass, from $11.0 < \log_{10}[M_{\star}({\rm M}_{\odot})] < 12.5$, peaking at $\log_{10}[M_{\star}({\rm M}_{\odot})] = 11.5$.

As discussed at length in the previous section, we use the *r*-band output parameters to characterize our BCGs. There is, however, little variation in the two as both bands pick-up light from predominantly the same stellar populations (e.g. Kennedy et al. 2016; Taylor-Mager et al. 2007). We display comparisons between morphological parameter outputs for *g*/*i* with *r* in Fig. 11 to illustrate this point. Moreover, as shown in Fig. A2, the overall scatter in the *i*-band output at 17th magnitude or brighter compared to input is reasonably small (e.g. $\Delta m_{\rm i} \sim 0.2$ at $m_{\rm i} = 17$); this result is also likely to be a worst-case scenario, given that the peak output *i*-band magnitude for our BCGs is ∼0.6 mag brighter than for the *r* band.

4.2 The influence of stellar mass on BCG structure

To determine which parameters are the primary drivers behind the correlations in our data, we have performed a Spearman rank analysis on our main sample (Table 3). We have also provided a partial Spearman analysis as well to test the robustness of our results against selection effects, which is summarized in Appendix B for

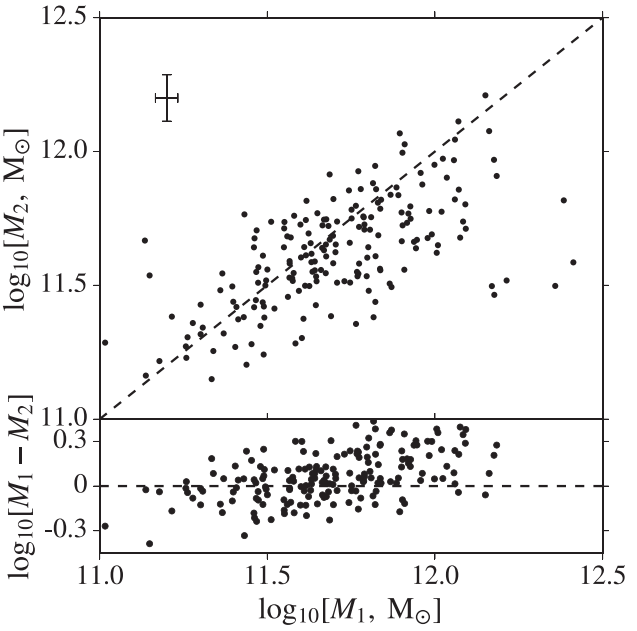

Figure 10. Comparison between the stellar mass estimates for our BCGs using a scaling relation from Taylor et al. (2011) and those in the MPA–JHU value-added catalogue, for a common sample of 192 BCGs (x- and y-axes, respectively). The crosshairs give the typical error value in each respective axis (for the MPA–JHU catalogue, drawn from the 16th and 84th percentile estimates).

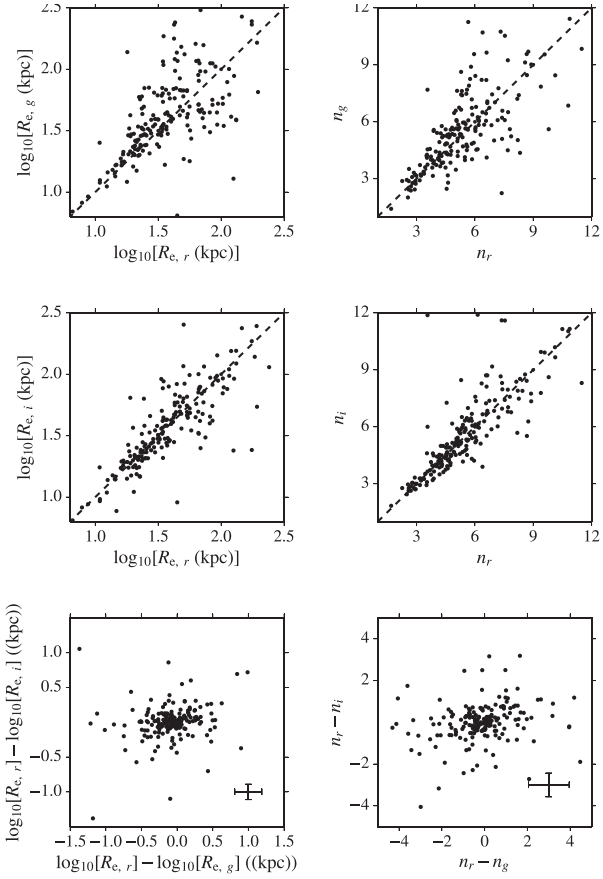

Figure 11. Comparison between the output structural parameters for the BCG sample (N=198). The dashed line represents the 1:1 relation and the crosshairs in the bottom two plots represent the 1σ scatter in x/y. In general, there is a good agreement across bands, albeit with increased scatter at large n/R_e. This has also been demonstrated in our simulations (Section3.4).

the parameters of interest (Tables B1–B7; computed using MATLAB's 'PARTIALCORR' routine), following a similar practice to Collins & Mann (1998). We hold our significance level at the standard value of $p \leq 0.05$ throughout ($\log_{10}[p_s] \leq -1.301$).

Fig. 12 suggests a strong correlation between the effective radius and stellar mass (luminosity) of our objects (Spearman rank coefficient, $r_s = 0.65$ and $\log_{10}[p_s] < -45$), which remains largely unchanged when any dependence on the environmental parameters are removed (see Tables B2, B3, and B6). Indeed, this behaviour is also seen in Fig. 13, which we discuss in detail in the upcoming section. These results indicate that the mass–size relation for BCGs seen here largely appears to exist independently of environment; this was also concluded by Zhao et al. (2015b). These observations support the scenario proposed by Shankar et al. (2014), who provided a semi-analytic model of BCG evolution since $z \sim 0.3$ and found no major environmental dependence on the sizes of early-type central galaxies (see Section 2.2). Indeed, numerous other studies have found this to be true of cluster galaxies in general at $z < 1$. For example, Kelkar et al. (2015) modelled galaxies in a similar way to this work in the ESO distant cluster survey (White et al. 2005), a *Hubble Space Telescope* survey of 20 cluster fields from $0.4 < z < 0.8$. Splitting the sample into to cluster and field galaxies using a threshold in velocity dispersion, they found no differences in the sizes of galaxies inside or outside of the cluster. Huertas-Company et al. (2013) reported similar findings in their work, reporting a doubling of massive ellipticals (including BCGs) in size from $z \sim 1$ to present, but no environmental dependence on the mass–size relation.

The corresponding $R_e - M_\star$ relation from Shen et al. (2003) derived for a general population of early-type galaxies independent of environment (defined as $n > 2.5$) has also been included for comparison. Our BCGs lie significantly above this relation (∼0.5 dex). Zhao et al. (2015b) came to a similar conclusion in their work, finding that most of their BCGs lay significantly above this relation, especially for BCGs which they classified morphologically as 'cD' types. The more massive and extended nature of BCGs in comparison to elliptical non-BCGs has been also found by numerous other studies since $z \sim 1$ (von der Linden et al. 2007, Vulcani et al. 2014, Bernardi 2009), although some argue that, when matched in colour and mass, there are few differences between BCGs and their satellites (e.g. Guo et al. 2009).

Comparing with the correlation between mass and effective radius, we also find a weaker correlation between stellar mass and Sérsic index ($r_s = 0.1548$ and $\log_{10}[p_s] = -1.536$). The consistency of the BCGs in our sample is likely due to the fact that they all have early-type morphologies and are bulge-dominated (sample median $n = 5.26 \pm 2.07$). Some studies have found correlations between n and $M_\star$ (e.g. Guo et al. 2009); however, Zhao et al. (2015b) reported that this relation is driven by the strong dependence of n on R_e than any separate dependence of mass on Sérsic index (rightmost panel of Fig. 12, $r_s = 0.58$ and $\log_{10}[p_s] < -45$), finding that this relation disappeared when they chose to use SED-based masses (though their conclusions were otherwise unchanged when they used a scaling relation). They did however find a visual morphological dependence on Sérsic index when they split their sample into E- and cD-type BCGs. Indeed, this weak, positive correlation

Table 3. Full Spearman rank analysis for all the variables examined in this study for the *r*-band morphological parameters. The top half of the table lists the Spearman rank correlation coefficient (r_s), whereas the bottom half of the table provides the log of its corresponding *p*-value ($\log_{10}[p_s]$).

	R_e	L_X	M_{200}	n	$M_\star$	λ	z
R_e	–	0.26711	0.11014	0.58263	0.64668	0.12535	0.30716
L_X	−3.8404	–	0.43005	−0.14079	0.39447	0.54933	0.57387
M_{200}	−0.91578	−9.4719	–	−0.14423	0.26984	0.51566	0.29608
n	<−45	−1.3244	−1.3749	–	0.1548	−0.10605	−0.059135
$M_\star$	<−45	−7.9602	−3.911	−1.536	–	0.24395	0.50075
λ	−1.1095	−16.356	−14.187	−0.86639	−3.2872	–	0.30286
z	−4.9478	<−45	−4.6253	−0.39105	<−45	−4.8622	–

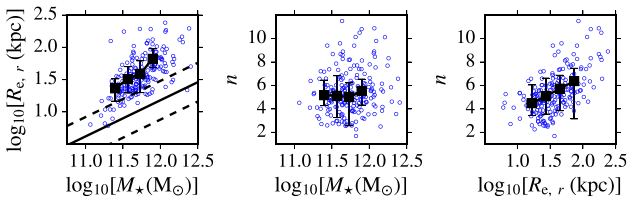

Figure 12. Correlations between the BCG structural parameters. For clarity, the data have been binned using a Scott's-rule optimized bin width to illustrate structure (omitting bins with fewer than 15 objects). The error bars mark the 16th and 84th percentiles of each bin. The solid line is the relation for SDSS 'early-type' galaxies ($n > 2.5$) from Shen et al. (2003), with the dashed lines marking the 1σ scatter.

is removed by accounting for any R_e dependence through applying a partial Spearman (Table B1).

The prominent anticorrelation between n and $M_\star$ that then arises as a result of removing any dependence on R_e ($r_s = -0.3641$ and $\log_{10}[p_s] = -6.871$) could therefore be arise from two possible effects: a result of evolution, or underestimation of the slope due to surface-brightness effects which was also demonstrated by our simulations (Fig. 7). From our simulations in Section 3.4, we believe it is more likely that the latter is the cause behind the observed scatter in this relation, due to some contamination with a number of profiles suffering from this effect. Indeed, when fixing for redshift, there is no anticorrelation present (TableB7, $r_s = 0.2000$, $\log_{10}[p_s] = -2.321$). At the very least underestimating the slope cannot be ruled out as the source of the anticorrelation; nevertheless, although we observe an increased scatter in R_e and magnitude at decreasing surface brightness, we see no evidence for any real change in direction of the bias (Fig. 7). It is worth noting that Stott et al. (2011) also reported no evolutionary dependence on BCG profile slope between $0.25 < z < 1$ from their Sérsic fits; Ascaso et al. (2011) measured a change in size from $0 < z < 0.6$, but also no prominent change in profile slope. In contrast, Bernardi (2009) did find that BCGs are more massive and extended than field or non-BCG satellite galaxies; however, Weinmann et al. (2009), using SDSS data, found little difference. Discrepancies between results therefore appear to lie in the method of selection, the method of defining environment and whether to take a single or multiple-component approach when fitting.

4.3 How do the characteristics of BCGs relate to their environment?

We compare the properties of our BCGs with that of their host cluster environments in Fig. 13. It is immediately obvious that the masses of our BCGs are significantly correlated with all three environmental properties at the focus of this study; however, the

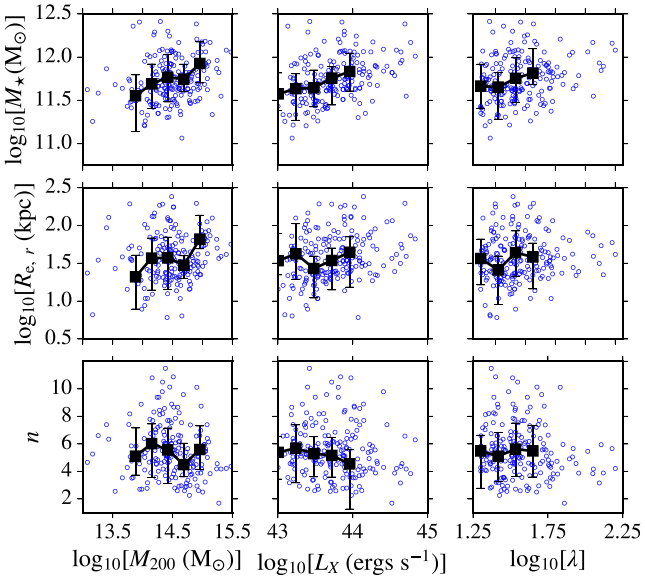

Figure 13. Correlations between the environmental parameters outlined in this study with BCG structural parameters and stellar mass. Bins are shown with $N \geq 15$ objects. The correlation between BCG mass and the properties of the host cluster appear more compelling than with the structural parameters, where we observe few significant correlations (see Table 3 and partial Spearman analysis in Appendix B).

strength of the correlation largely varies depending on the property of interest (see Table 3). The stellar masses of our BCGs are the most strongly correlated with X-ray luminosity ($r_s = 0.394$ and $\log_{10}[p_s] = -7.9602$) and are the least correlated with richness ($r_s = 0.244$ and $\log_{10}[p_s] = -3.287$). Zhao et al. (2015b) found a similar result with their BCGs, in that they measured a correlation between BCG stellar mass and cluster dynamical mass, albeit with large scatter (Pearson rank coefficient = 0.17, see the paper for details). They provided arguments against the correlation being caused due to more massive haloes being populated by more massive BCGs simply by chance, due to the dominance of BCGs in comparison to the general population of cluster galaxies (e.g. von der Linden et al. 2007).

All three environmental parameters, although measured independently, suffer from some degeneracy (more massive haloes are generally more likely to be occupied by a larger number of galaxies and contain a larger amount of bound ICM, e.g. Leauthaud et al. 2010; White et al. 2011; Mehrtens et al. 2016), the relevant environmental correlations are shown for reference in Fig. 14. To address potential selection biases which may arise with redshift (e.g. Fig. 2), we t2est our correlations independently of redshift (TableB7) to analyse the robustness of our results. When doing so, we find our correlations

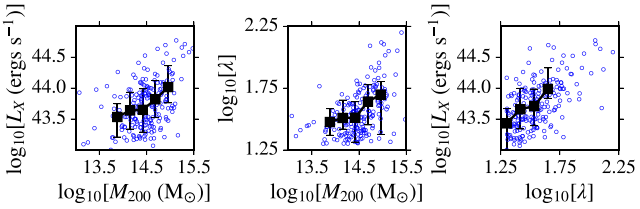

Figure 14. Correlations between characteristics of the host cluster (bins shown with $N \geq 15$ objects). The physical properties of clusters are highly correlated; hence the importance of accounting for selection.

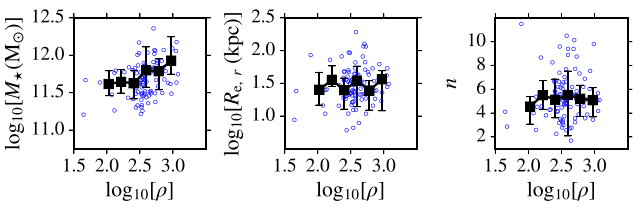

Figure 15. Correlations between luminosity-weighted environmental density, $\log_{10}[\rho]$, with BCG properties (bins shown with $N \geq 5$ objects) for 102 BCGs in common with the catalogues of Tempel, Tago & Liivamägi (2012). As before, there is a correlation with mass, but no correlation with the structural parameters.

remain (albeit at reduced strength) for both X-ray luminosity ($r_s = 0.16$ and $\log_{10}[p_s] = -1.61$) and cluster mass ($r_{sn} = 0.14$ and $\log_{10}[p_s] = -1.37$), but not for richness, which drops below significance ($r_s = 0.1$ and $\log_{10}[p_s] = -0.8$). We discuss our interpretation of the lack of correlation with richness below.

As shown in Fig. 14, the X-ray luminosity of a cluster is clearly dependent on mass and is often used as an alternative proxy for the former. However, depending on the dynamical state of the cluster, such measurements are prone to their own biases (e.g. Nagai, Vikhlinin & Kravtsov 2007). Relaxed, highly evolved clusters have been found generally to be more likely to host an X-ray luminous cool core than clusters out of dynamical relaxation; indeed, the degree of offset of the BCG correlates inversely with the X-ray luminosity of a cluster (e.g. Sanderson, Edge & Smith 2009; Stott et al. 2012). It would therefore follow that one of the drivers behind the strength of this relation is the tendency of more massive BCGs to be located within clusters with a greater degree of dynamical relaxation and structural evolution, potentially where the degree of 'dominance' of the BCG is large (e.g. Jones et al. 2003). Of course, there are physical mechanisms that add further complications to this assumption; an increased abundance of radio-loud AGN has been found in BCGs residing in cool-core clusters (e.g. Burns 1990; Crawford et al. 1999), the feedback from which are thought to be capable of heating the ICM (e.g. McNamara et al. 2014; Russell et al. 2014; Best et al. 2007).

There is, as mentioned in Section 4.1, little evidence for any independent environmental dependence on the scale sizes of our BCGs from mass. Although there is an apparent correlation with X-ray luminosity on effective radius ($r_s = 0.26711$ and $\log_{10}[p_s] = -3.8404$), it entirely disappears at fixed stellar mass ($r_s = 0.028219$ and $\log_{10}[p_s] = -0.1592$); suggesting that stellar mass rather than effective radius is the main driver behind the observed correlation. A similar conclusion was reached by Zhao et al. (2015b) who also found, after visually classifying their BCGs into E and cD types ('bulge only' versus 'bulge+envelope', see Zhao et al. 2015a for the classification method), that cD types constitute a significantly more massive and extended population than E types. Zhao et al. (2015b) also reported a weak environmental dependence on their visual morphologies, with cD-type BCGs generally inhabiting marginally more massive, denser haloes than E-type BCGs. A larger fraction of BCGs with cD-type haloes were found by Brough et al. (2005) to reside in more X-ray luminous clusters. As we do not visually classify our BCGs due to the fact we are unlikely to possess the necessary photometric depth, we cannot provide a direct comparison; nevertheless, it would be interesting to explore large epochs of cosmic history to determine if this morphological dependence holds at higher redshift. Next-generation surveys, such as the Large Synoptic Survey Telescope which constitute both large volumes and deep photometry may be the key for solving such problems (e.g. Ivezic et al. 2008).

As aforementioned, cluster richness, of the properties featured in this work, is the least significantly correlated with BCG properties, with no significant correlation present with stellar mass independently of redshift. This result may arise because it represents a weaker means of quantifying environment, in that it is simply a proxy for the number of galaxies attributed to a cluster. A richness value provides minimal information about the nature of the cluster galaxies; the influence of several neighbours of comparable mass to a BCG would likely have a larger influence than an equal number of much smaller neighbours, nevertheless the richness estimators in each case would be equivalent (e.g. Bautz & Morgan 1970 provided a basic classification scheme for galaxy clusters with this issue in mind). However, the richness values can be used to provide a robust measure of the total stellar mass of a cluster when coupled with abundance matching, as demonstrated by Old et al. (2015).

Arguably, a more physically motivated measure of environment for our purposes than richness would take overall luminosities of galaxies within a cluster into account; this point was also raised by Zhao et al. (2015a). Such a measure is shown in Fig. 15 using the luminosity-weighted environmental density maps of Tempel et al. (2012), smoothed to scales of 1 Mpc h^{-1}. The maps are computed from SDSS DR8 data and constitute the largest contiguous region of the SDSS footprint; we matched the SPIDERS BCGs with the catalogues within 3 arcsec, finding 102 common objects which had a corresponding measurement of environmental density. Although we cannot provide a complete comparison as we lack coverage for the full sample of objects, the result appears promising. In common with Fig. 13, there is a significant correlation between environmental density and BCG stellar mass ($r_s = 0.3233$ and $\log_{10}[p_s] = -3.0128$), but no correlation between either effective radius or Sérsic index (Spearman rank correlation coefficients for n and R_e 0.1369 and 0.0117. respectively, with corresponding $\log_{10}[p_s]$ values of -0.6185 and -0.7701). Even after accounting for the strong L_X dependence through our partial Spearman analysis, the correlation between BCG mass and environmental density remains significant ($r_s = 0.2554$ and $\log_{10}[p_s] = -2.0023$), as does the $L_X - M_\star$ relation when controlling for environmental density ($r_s = 0.3150$ and $\log_{10}[p_s] = -2.8811$). This result suggests that our sample contains a significant fraction of clusters which are mature systems (i.e. self-contained, virialized), having accumulated the majority of their stellar component up to $z \sim 0.3$.

5 DISCUSSION

At fixed stellar mass, we do not measure any significant anticorrelation between redshift and scale size for our sample (Table B5); this therefore suggests that there is little overall evolution in the scale size of our BCGs. Due to the large number of rich, high-mass clus-

ters in our sample compared with group-level systems, it is likely that many of the clusters in our sample are nearing maturity; this is reflected by the relatively homogeneous properties of the BCGs observed here. Our findings here are consistent with Stott et al. (2011), who also used an X-ray-selected cluster sample similar in redshift and cluster X-ray luminosity to the SPIDERS sample. It also appears that any environmental dependence on the size–stellar mass relation for BCGs is minimal for our sample at the redshift and halo mass range of this study (median $M_{200} = 1.4 \times 10^{14}\,\mathrm{M}_{\odot}$). Stellar mass, over the environmental properties featured in this study, arises as the more important factor governing BCG morphology. For example, Guo et al. (2009), reporting a similar result in their work, interpreted the lack of an obvious $n{-}M_{200}$ relation as indicating that there is no clear mass threshold where a dark matter halo is capable of producing spheroidal centrals. However, they found a strong trend between stellar mass and Sérsic index. This claim was disputed by Zhao et al. (2015a), who found no such trend; however, they also found little environmental dependence on the structural parameters of BCGs up to $z \sim 0.1$ when their sample was not split by visual morphology.

Here, our findings suggest a trend between $n{-}M_{\star}$; though in general, we make the simplifying assumption due to the higher peak redshift of our BCGs that they are single-component objects, and therefore do not attempt to fit a bulge+disc. As we have demonstrated in our simulations in Section 3.4, $n = 1$, 'disc-like' profiles demonstrate unpredictable behaviour more rapidly than 'bulge-like', higher n profiles. It would therefore, at the magnitude range of the BCGs in this study, be difficult to draw any meaningful conclusions from fitting a dual component profile (e.g. Sérsic+exponential) for any but the most luminous galaxies in our study. As wide surveys with significantly deeper photometry become readily available over the next decade, they would be an ideal test bed at higher redshift to examine the observed dual-component nature of some BCGs seen at $z < 0.1$ (e.g. Huang et al. 2017), and, by extension, the build-up of the ICL.

It follows that, if the BCGs in our sample display little morphological dependence with environment, any influence of environment on their evolution must have been apparent at an earlier point in the assembly process. Due to the fact that our BCGs are more massive and extended than the general population of $n > 2.5$ elliptical galaxies (Section 4), the cluster potential well must have some influence in the past on the formation of BCGs. For example, the work of von der Linden et al. (2007) found BCGs to have a higher dynamical-to-stellar mass ratio, indicating that they contained a larger fraction of dark matter compared to a sample of colour-matched non-BCG galaxies taken from the SDSS.

Various studies have predicted the growth in stellar mass of BCGs, with a wide range of results predicting BCGs doubling in size since $z \sim 0.3$ to predicting size growth of less than 20 per cent since $z \sim 1$ (e.g. Bernardi 2009; Ascaso et al. 2011; Stott et al. 2011; Vulcani et al. 2014). The discrepancies lie not only in the method of measurement (e.g. single profile-modelling versus dual-profile modelling, to account for the stellar halo seen in BCGs), but also the method of sample selection; an early study, Collins et al. (2003), argued that the growth rates seen in X-ray luminous clusters are modest since $z \sim 1$, with larger rates present in clusters with low X-ray luminosities. The early build-up of stellar mass in BCGs (e.g. Collins et al. 2009) as well as observations of an established red sequence in clusters at $z > 1.5$ (e.g. Cooke et al. 2016) still present a challenge to simulations, some of which predict a large mass increase in BCGs between $0 < z < 1$ (e.g. De Lucia & Blaizot 2007 predicted a fourfold increase during this time-scale). An improved understanding of the formation of the ICL, such as the stripping of stars from central galaxies during the cluster assembly process, is therefore required to understand the ongoing discrepancies between simulations and observations of BCGs (e.g. Burke et al. 2012; Burke, Hilton & Collins 2015).

6 CONCLUSIONS

We created a sample of 329 BCGs from the X-ray-selected SPIDERS clusters survey, and investigated three cluster properties of interest: X-ray luminosity, richness, and halo mass, the last property of which we estimated through the cluster velocity dispersion. We modelled our BCGs with single-Sérsic profiles using the SIGMA pipeline. We tested the ability of our pipeline to recover parameters from SDSS data using 10^4 model profiles, outlining a final science sample of 198 BCGs. Finding the results of our best-fitting parameters to be generally consistent across bands, we derived stellar masses for our BCGs based on Taylor et al. (2011). We conclude the following:

(i) Our simulations suggest a strong codependency between n, R_{e}, and apparent magnitude.

(ii) We detected a negative bias in Sérsic index with effective radius, as a result of the degeneracy between the background level and profile wings. We also found a significant increase in the scatter of output effective radii at fainter magnitudes. This behaviour occurred regardless of band or input Sérsic index/effective radius. We used this information to approximate the fitting magnitude limit of our sample ($m_{\mathrm{r}} = 16.5$).

(iii) The scale sizes of the BCGs in our sample are highly correlated with their stellar masses, in common with numerous other studies (Section 4). The BCGs are also significantly more massive and extended than the general $n > 2.5$ population of galaxies in the SDSS.

(iv) There is a weak correlation between BCG mass and Sérsic index, inferring that more massive BCGs may tend towards having slightly more centrally concentrated light profiles.

(v) Significant correlations exist between the masses of our BCGs and all three of the cluster properties explored in this study (richness, cluster mass, and X-ray luminosity). However, fixing for redshift, we do not find any significant correlation with richness – indicating that it is likely to be less useful measure of environment in this context.

(vi) There is no evidence that environment, at the redshift of our clusters, has any influence over the size–stellar mass relation of our BCGs, nor is there evidence for any correlation between the profile slopes of our BCGs and the cluster environment.

(vii) For a reduced sample of 102 BCGs, the environmental density is highly correlated with stellar mass, but no correlation is present with either structural parameter. A partial Spearman analysis reveals this correlation to be largely independent of X-ray luminosity.

The picture is therefore that BCGs, in rich, X-ray-selected clusters appear to have no significant environmental dependence on their structures, independently of their mass, up to $z \sim 0.3$. If the primary driver behind growth of BCGs is indeed through multiple mergers (e.g. Ostriker & Tremaine 1975), it is likely that within the M_{200} range of the clusters explored here, the mass assembly has predominantly occurred at earlier times, with growth slowing due to the large dynamical friction time-scales associated with massive clusters at late times. Our work supports the scenario of the homogeneity presented by BCGs in massive clusters up to inter-

mediate redshifts (e.g. Collins & Mann 1998; Collins et al. 2009; Whiley et al. 2008; Stott et al. 2011). The full catalogue of objects is published electronically; a description of catalogue parameters is included in Appendix C.

ACKNOWLEDGEMENTS

We thank the anonymous referee for their insightful comments that greatly improved the clarity of the paper. KEF is supported by a Science and Technologies Funding Council (STFC) award. CAC, IKB, and LSK are supported by an STFC research grant (ST/M000966/1). KEF would also like to personally thank the SPIDERS and CODEX teams for their cooperation, collaboration and support throughout this work. KEF would also like to thank LSK for his consistent advice, support, and enabling the use of the software throughout this project.

This paper makes use of data from the SDSS. Funding for the SDSS-IV has been provided by the Alfred P. Sloan Foundation, the U.S. Department of Energy Office of Science, and the Participating Institutions. SDSS acknowledges support and resources from the Center for High-Performance Computing at the University of Utah. The SDSS web site is www.sdss.org.

SDSS is managed by the Astrophysical Research Consortium for the Participating Institutions of the SDSS Collaboration including the Brazilian Participation Group, the Carnegie Institution for Science, Carnegie Mellon University, the Chilean Participation Group, the French Participation Group, Harvard-Smithsonian Center for Astrophysics, Instituto de Astrofísica de Canarias, The Johns Hopkins University, Kavli Institute for the Physics and Mathematics of the Universe/University of Tokyo, Lawrence Berkeley National Laboratory, Leibniz Institut für Astrophysik Potsdam, Max-Planck-Institut für Astronomie (Heidelberg), Max-Planck-Institut für Astrophysik (Garching), Max-Planck-Institut für Extraterrestrische Physik, National Astronomical Observatories of China, New Mexico State University, New York University, University of Notre Dame, Observatório Nacional/MCTI, The Ohio State University, Pennsylvania State University, Shanghai Astronomical Observatory, United Kingdom Participation Group, Universidad Nacional Autónoma de México, University of Arizona, University of Colorado Boulder, University of Oxford, University of Portsmouth, University of Utah, University of Virginia, University of Washington, University of Wisconsin, Vanderbilt University, and Yale University.

REFERENCES

Aihara H. et al., 2011, ApJS, 193, 29
Alam S. et al., 2015, ApJS, 219, 12
Aragon-Salamanca A., Baugh C. M., Kauffmann G., 1998, MNRAS, 297, 427
Ascaso B., Aguerri J. A. L., Varela J., Cava A., Bettoni D., Moles M., D'Onofrio M., 2011, ApJ, 726, 69
Bautz L. P., Morgan W. W., 1970, ApJ, 162, L149
Beers T. C., Flynn K., Gebhardt K., 1990, AJ, 100, 32
Bernardi M., 2009, MNRAS, 395, 1491
Bernardi M., Hyde J. B., Sheth R. K., Miller C. J., Nichol R. C., 2007, AJ, 133, 1741
Bernardi M., Meert A., Vikram V., Huertas-Company M., Mei S., Shankar F., Sheth R. K., 2014, MNRAS, 443, 874
Bertin E., 2013, Astrophysics Source Code Library, record ascl:1301.001
Bertin E., Arnouts S., 1996, A&AS, 117, 393
Best P. N., von der Linden A., Kauffmann G., Heckman T. M., Kaiser C. R., 2007, MNRAS, 379, 894
Bhavsar S. P., Barrow J. D., 1985, MNRAS, 213, 857
Blanton M. R., Kazin E., Muna D., Weaver B. A., Price-Whelan A., 2011, AJ, 142, 31
Blanton M. R., Lin H., Lupton R. H., Maley F. M., Young N., Zehavi I., Loveday J., 2003, AJ, 125, 2276
Blanton M. R. et al., 2017, AJ, 154, 28
Brinchmann J., Charlot S., White S. D. M., Tremonti C. , Kauffmann G., Heckman T. , Brinkmann J. , 2004, MNRAS, 351, 1151
Brough S., Collins C. A., Burke D. J., Lynam P. D., Mann R. G., 2005, MNRAS, 364, 1354
Bruzual G., Charlot S., 2003, MNRAS, 344, 1000
Burke C., Collins C. A., Stott J. P., Hilton M., 2012, MNRAS, 425, 2058
Burke C., Hilton M., Collins C., 2015, MNRAS, 449, 2353
Burns J. O., 1990, AJ, 99, 14
Böhringer H. et al., 2001, A&A, 369, 826
Caldwell C. E., McCarthy I. G., Baldry I. K., Collins C. A., Schaye J., Bird S., 2016, MNRAS, 462, 4117
Carlberg R. G., Yee H. K. C., Ellingson E., Abraham R., Gravel P., Morris S., Pritchet C. J., 1996, ApJ, 462, 32
Chabrier G., 2003, PASP, 115, 763
Chilingarian I. V., Melchior A.-L., Zolotukhin I. Y., 2010, MNRAS, 405, 1409
Cibirka N. et al., 2016, MNRAS, 468, 1092,
Ciotti L., 1991, A&A, 249, 99
Clerc N. et al., 2016, MNRAS, 463, 4490
Collins C., Brough S., Burke D., Mann R., Lynam P., 2003, Ap&SS, 285, 51
Collins C. A., Guzzo L., Nichol R. C., Lumsden S. L., 1995, MNRAS, 274, 1071
Collins C. A., Mann R. G., 1998, MNRAS, 297, 128
Collins C. A. et al., 2009, Nature, 458, 603
Cooke E. A. et al., 2016, ApJ, 816, 83
Crawford C. S., Allen S. W., Ebeling H., Edge A. C., Fabian A. C., 1999, MNRAS, 306, 857
Dawson K. S. et al., 2016, AJ, 151, 44
De Lucia G., Blaizot J., 2007, MNRAS, 375, 2
de Vaucouleurs G., 1948, Ann. Astrophys., 11, 247
Djorgovski S., Davis M., 1987, ApJ, 313, 59
Donzelli C. J., Muriel H., Madrid J. P., 2011, ApJS, 195, 15
Driver S. P. et al., 2011, MNRAS, 413, 971
Edge A. C., 2001, MNRAS, 328, 762
Erwin P., 2015, ApJ, 799, 226
Fabian A. C., Crawford C. S., Edge A. C., Mushotzky R. F., 1994, MNRAS, 267, 779
Fabian A. C., Nulsen P. E. J., 1977, MNRAS, 180, 479
Fabian A. C., Sanders J. S., Allen S. W., Crawford C. S., Iwasawa K., Johnstone R. M., Schmidt R. W., Taylor G. B., 2003, MNRAS, 344, L43
Finn R. A. et al., 2005, ApJ, 630, 206
Finoguenov A. et al., 2007, ApJS, 172, 182
Fitzpatrick E. L., 1999, PASP, 111, 63
Freeman K. C., 1970, ApJ, 160, 811
Fukugita M., Ichikawa T., Gunn J. E., Doi M., Shimasaku K., Schneider D. P., 1996, AJ, 111, 1748
George M. R. et al., 2012, ApJ, 757, 2
Gonzalez A. H., Zaritsky D., Zabludoff A. I., 2007, ApJ, 666, 147
Graham A., Lauer T. R., Colless M., Postman M., 1996, ApJ, 465, 534
Graham A. W., Driver S. P., 2005, PASA, 22, 118
Green T. S. et al., 2016, MNRAS, 461, 560
Gunn J. E. et al., 2006, AJ, 131, 2332
Guo Y. et al., 2009, MNRAS, 398, 1129
Hikage C., Mandelbaum R., Leauthaud A., Rozo E., Rykoff E. S., 2017, preprint (arXiv:1702.08614)
Hill D. T. et al., 2011, MNRAS, 412, 765
Huang S., Leauthaud A., Greene J., Bundy K., Lin Y.-T., Tanaka M., Miyazaki S., Komiyama Y., 2017, MNRAS, 475, 3348
Hudson D. S., Mittal R., Reiprich T. H., Nulsen P. E. J., Andernach H., Sarazin C. L., 2010, A&A, 513, A37
Huertas-Company M. et al., 2013, MNRAS, 428, 1715

Häußler B. et al., 2013, MNRAS, 430, 330
Ivezic Z. et al., 2008, preprint, (arXiv:0805.2366)
Johansson P. H., Naab T., Ostriker J. P., 2012, ApJ, 754, 115
Jones L. R., Ponman T. J., Horton A., Babul A., Ebeling H., Burke D. J., 2003, MNRAS, 343, 627
Karman W. et al., 2015, A&A, 574, A11
Kauffmann G. et al., 2003, MNRAS, 346, 1045
Kelkar K., Aragón-Salamanca A., Gray M. E., Maltby D., Vulcani B., De Lucia G., Poggianti B. M., Zaritsky D., 2015, MNRAS, 450, 1246
Kelvin L. S. et al., 2012, MNRAS, 421, 1007
Kennedy R. et al., 2016, MNRAS, 460, 3458
Kroupa P., 2001, MNRAS, 322, 231
Lange R. et al., 2016, MNRAS, 462, 1470
Laporte C. F. P., White S. D. M., 2015, MNRAS, 451, 1177
Lauer T. R., 1988, ApJ, 325, 49
Lea S. M., Silk J., Kellogg E., Murray S., 1973, ApJ, 184, L105
Leauthaud A. et al., 2010, ApJ, 709, 97
Lin Y.-T., Mohr J. J., 2004, ApJ, 617, 879
Liu F. S., Xia X. Y., Mao S., Wu H., Deng Z. G., 2008, MNRAS, 385, 23
Loubser S. I., Sánchez-Blázquez P., Sansom A. E., Soechting I. K., 2009, MNRAS, 398, 133
Markevitch M., Gonzalez A. H., David L., Vikhlinin A., Murray S., Forman W., Jones C., Tucker W., 2002, ApJ, 567, L27
Maughan B. J., Giles P. A., Rines K. J., Diaferio A., Geller M. J., Van Der Pyl N., Bonamente M., 2016, MNRAS, 461, 4182
McCarthy I. G., Schaye J., Bird S., Le Brun A. M. C., 2016, MNRAS, 465, 2936,
McNamara B. R. et al., 2014, ApJ, 785, 44
Mehrtens N. et al., 2016, MNRAS, 463, 1929
Merritt D., 1985, ApJ, 289, 18
Mihos J. C., Harding P., Feldmeier J., Morrison H., 2005, ApJ, 631, L41
Miller C. J. et al., 2005, AJ, 130, 968
Mink D. J., 1998, AAS/Division of Dynamical Astronomy Meeting, 1144
Moffat A. F. J., 1969, A&A, 3, 455
Morgan W. W., Lesh J. R., 1965, ApJ, 142, 1364
Nagai D., Vikhlinin A., Kravtsov A. V., 2007, ApJ, 655, 98
Navarro J. F., Frenk C. S., White S. D. M., 1996, ApJ, 462, 563
Old L. et al., 2015, MNRAS, 449, 1897
Oliva-Altamirano P. et al., 2017, AJ, 153, 89
Ostriker J. P., Tremaine S. D., 1975, ApJ, 202, L113
O'Dea C. P. et al., 2008, ApJ, 681, 1035
Peng C. Y., Ho L. C., Impey C. D., Rix H.-W., 2010, AJ, 139, 2097
Peterson J. R., Fabian A. C., 2006, Phys. Rep., 427, 1
Pillepich A., Porciani C., Reiprich T. H., 2012, MNRAS, 422, 44
Powell M. C., Urry C. M., Cardamone C. N., Simmons B. D., Schawinski K., Young S., Kawakatsu M., 2017, ApJ, 835, 22
Ragone-Figueroa C., Granato G. L., Murante G., Borgani S., Cui W., 2013, MNRAS, 436, 1750
Robotham A. S. G., Taranu D. S., Tobar R., Moffett A., Driver S. P., 2017, MNRAS, 466, 1513
Robotham A. S. G. et al., 2011, MNRAS, 416, 2640
Russell H. R. et al., 2014, ApJ, 784, 78
Rykoff E. S. et al., 2012, ApJ, 746, 178
Rykoff E. S. et al., 2014, ApJ, 785, 104
Rykoff E. S. et al., 2016, ApJS, 224, 1
Sanderson A. J. R., Edge A. C., Smith G. P., 2009, MNRAS, 398, 1698
Schaye J. et al., 2015, MNRAS, 446, 521
Schlafly E. F., Finkbeiner D. P., 2011, ApJ, 737, 103
Schlegel D. J., Finkbeiner D. P., Davis M., 1998, ApJ, 500, 525
Schneider D. P., Gunn J. E., Hoessel J. G., 1983, ApJ, 264, 337
Schombert J. M., 1986, ApJS, 60, 603
Shankar F. et al., 2014, MNRAS, 439, 3189
Shen S., Mo H. J., White S. D. M., Blanton M. R., Kauffmann G., Voges W., Brinkmann J., Csabai I., 2003, MNRAS, 343, 978
Simard L., 1998, in Albrecht R., Hook R. N., Bushouse H. A., eds, ASP Conf. Ser. Vol. 145, Astronomical Data Analysis Software and Systems VII, Astron. Soc. Pac., San Francisco. p. 108
Simmons B. D., Urry C. M., 2008, ApJ, 683, 644
Smee S. A. et al., 2013, AJ, 146, 32
Steinhauser D., Schindler S., Springel V., 2016, A&A, 591, A51
Stott J. P., Collins C. A., Burke C., Hamilton-Morris V., Smith G. P., 2011, MNRAS, 414, 445
Stott J. P., Edge A. C., Smith G. P., Swinbank A. M., Ebeling H., 2008, MNRAS, 384, 1502
Stott J. P. et al., 2012, MNRAS, 422, 2213
Stoughton C. et al., 2002, AJ, 123, 485
Sérsic J. L., 1963, Bol. Asoc. Argentina Astron. La Plata Argentina, 6, 41
Taylor-Mager V. A., Conselice C. J., Windhorst R. A., Jansen R. A., 2007, ApJ, 659, 162
Taylor E. N. et al., 2011, MNRAS, 418, 1587
Tempel E., Tago E., Liivamägi L. J., 2012, A&A, 540, A106
The Dark Energy Survey Collaboration 2005, preprint (arXiv)
Tonini C., Bernyk M., Croton D., Maraston C., Thomas D., 2012, ApJ, 759, 43
Tremonti C, et al., 2004, ApJ, 613, 898
van der Burg R. F. J. et al., 2017, A&A, 607, A79,
van der Wel A., Holden B. P., Zirm A. W., Franx M., Rettura A., Illingworth G. D., Ford H. C., 2008, ApJ, 688, 48
van Dokkum P. G. et al., 2008, ApJ, 677, L5
Vika M., Bamford S. P., Häußler B., Rojas A. L., Borch A., Nichol R. C., 2013, MNRAS, 435, 623
Vikhlinin A., Burenin R., Forman W. R., Jones C., Hornstrup A., Murray S. S., Quintana H., 2007, in Böhringer H., Pratt G. W., Finoguenov A., Schuecker P., eds, Heating versus Cooling in Galaxies and Clusters of Galaxies, Springer-Verlag, Berlin Heidelberg. p. 48
Vikram V., Wadadekar Y., Kembhavi A. K., Vijayagovindan G. V., 2010, MNRAS, 409, 1379
Vogelsberger M. et al., 2014, MNRAS, 444, 1518
Voges W. et al., 1999, A&A, 349, 389
Voit G. M., Meece G., Li Y., O'Shea B. W., Bryan G. L., Donahue M., 2016, ApJ, 845, 80
von der Linden A., Best P. N., Kauffmann G., White S. D. M., 2007, MNRAS, 379, 867
Vulcani B. et al., 2014, ApJ, 797, 62
Weinmann S. M., Kauffmann G., van den Bosch F. C., Pasquali A., McIntosh D. H., Mo H., Yang X., Guo Y., 2009, MNRAS, 394, 1213
Whiley I. M. et al., 2008, MNRAS, 387, 1253
White M. et al., 2011, ApJ, 728, 126
White S. D. M., Frenk C. S., 1991, ApJ, 379, 52
White S. D. M. et al., 2005, A&A, 444, 365
Yang X., Mo H. J., van den Bosch F. C., Jing Y. P., 2005, MNRAS, 356, 1293
York D. G. et al., 2000, AJ, 120, 1579
Zhao D., Aragón-Salamanca A., Conselice C. J., 2015a, MNRAS, 448, 2530
Zhao D., Aragón-Salamanca A., Conselice C. J., 2015b, MNRAS, 453, 4444

SUPPORTING INFORMATION

Supplementary data are available at *MNRAS* online.

furnell_bcg_table.ascii

Please note: Oxford University Press is not responsible for the content or functionality of any supporting materials supplied by the authors. Any queries (other than missing material) should be directed to the corresponding author for the article.

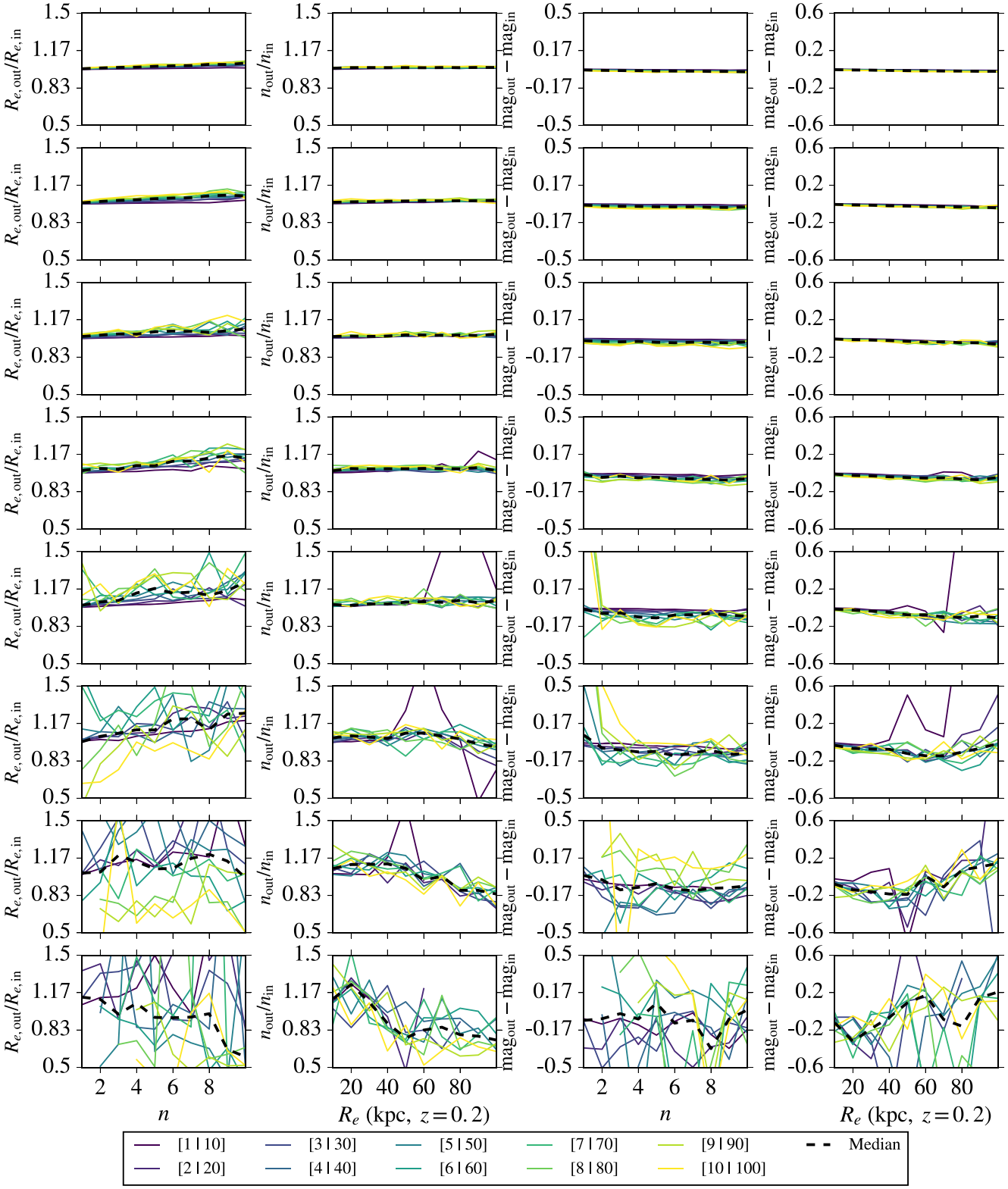

Figure A1. As in Fig. 7, but for the *g* band.

APPENDIX A: SIMULATED PROFILE OUTPUTS FOR *g*/*i*

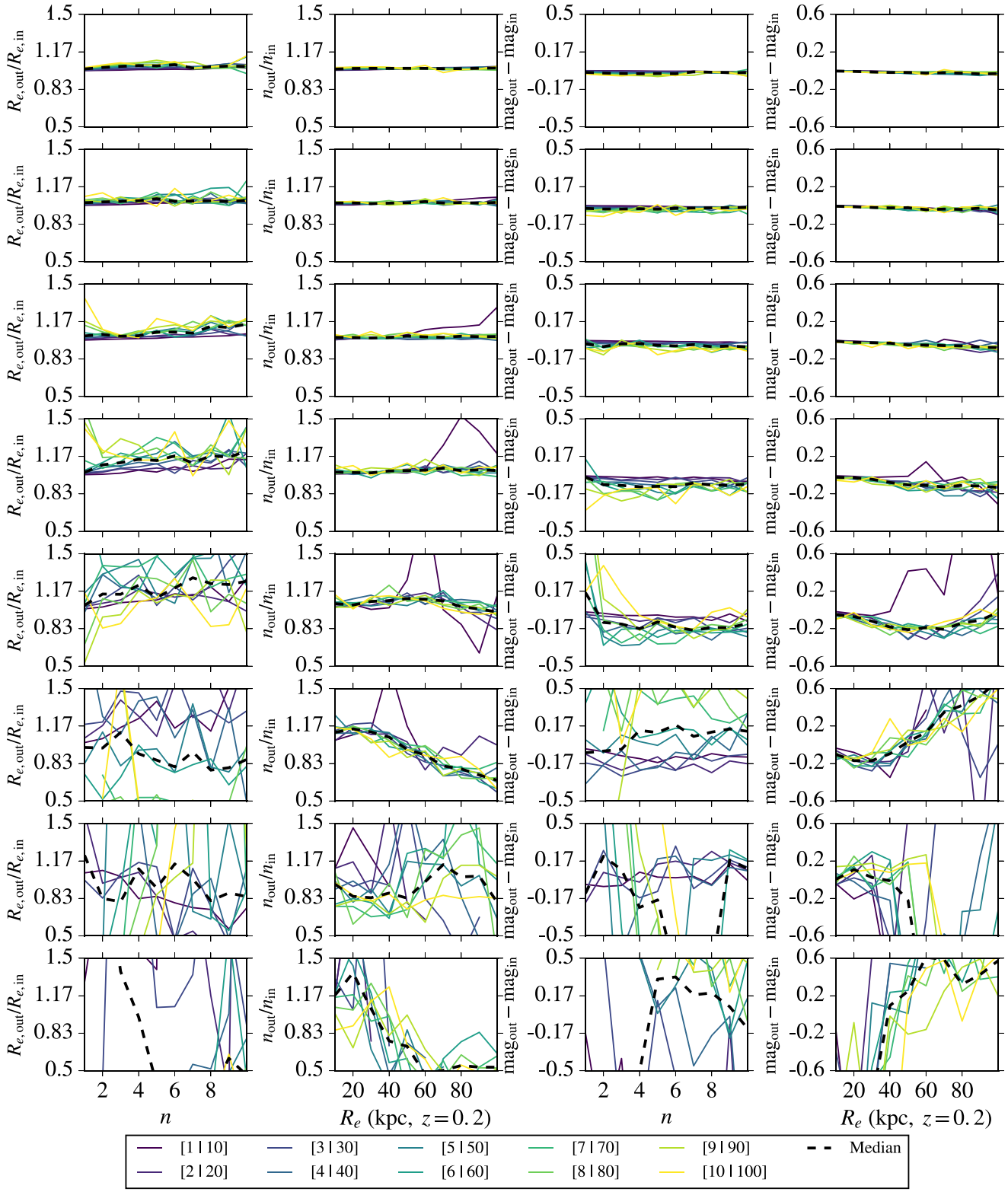

Figure A2. As in Fig. 7, but for the *i* band.

APPENDIX B: PARTIAL SPEARMAN ANALYSIS

Table B1. As in Table 3, but for fixed R_e.

	R_e	L_X	M_{200}	n	$M_\star$	λ	z
R_e	–	–	–	–	–	–	–
L_X	–	–	0.41439	−0.37348	0.3074	0.54307	0.53253
M_{200}	–	−8.8905	–	−0.27916	0.25043	0.48343	0.24611
n	–	−7.2236	−4.1668	–	−0.36407	−0.22452	−0.30248
$M_\star$	–	−4.9761	−3.4282	−6.871	–	0.21417	0.42349
λ	–	−15.858	−12.265	−2.8318	−2.6114	–	0.28225
z	–	−15.17	−3.3243	−4.8288	−9.2931	−4.2512	–

Table B2. As in Table 3, but for fixed L_X.

	R_e	L_X	M_{200}	n	$M_\star$	λ	z
R_e	–	–	−0.022206	0.64945	0.60292	−0.042913	0.20203
L_X	–	–	–	–	–	–	–
M_{200}	−0.12139	–	–	−0.12644	0.099939	0.33868	0.027848
n	−24.376	–	−1.1198	–	0.22026	−0.049023	0.032956
$M_\star$	−20.257	–	−0.7925	−2.7399	–	0.021243	0.37383
λ	−0.26097	–	−5.9754	−0.30733	−0.11553	–	−0.018234
z	−2.3652	–	−0.15681	−0.19054	−7.2367	−0.097594	–

Table B3. As in Table 3, but for fixed M_{200}.

	R_e	L_X	M_{200}	n	$M_\star$	λ	z
R_e	–	0.26515	–	0.61064	0.64182	0.082771	0.30621
L_X	−3.7962	–	–	−0.063337	0.34106	0.43534	0.5292
M_{200}	–	–	–	–	–	–	–
n	−20.894	−0.42555	–	–	0.19977	−0.033542	−0.0023672
$M_\star$	−23.651	−6.056	–	−2.3209	–	0.13708	0.47805
λ	−0.60848	−9.8358	–	−0.19451	−1.2666	–	0.20791
z	−4.9404	−14.958	–	−0.011621	−11.974	−2.4828	–

Table B4. As in Table 3, but for fixed n.

	R_e	L_X	M_{200}	n	$M_\star$	λ	z
R_e	–	0.44098	0.24644	–	0.69269	0.22933	0.42767
L_X	−10.102	–	0.41151	–	0.4339	0.54493	0.57356
M_{200}	−3.3321	−8.766	–	–	0.287	0.48069	0.26014
n	–	–	–	–	–	–	–
$M_\star$	−28.904	−9.7689	−4.3829	–	–	0.26129	0.52637
λ	−2.9377	−15.981	−12.116	–	−3.6976	–	0.30112
z	−9.4822	−17.987	−3.6684	–	−14.78	−4.7886	–

Table B5. As in Table 3, but for fixed $M_\star$.

	R_e	L_X	M_{200}	n	$M_\star$	λ	z
R_e	–	0.028219	−0.086562	0.6433	–	−0.045577	−0.014766
L_X	−0.1592	–	0.36228	−0.20772	–	0.51141	0.46609
M_{200}	−0.64727	−6.8054	–	−0.21471	–	0.45626	0.16035
n	−23.79	−2.4788	−2.6225	–	–	−0.15252	−0.14405
$M_\star$	–	–	–	–	–	–	–
λ	−0.28088	−13.863	−10.846	−1.4956	–	–	0.2169
z	−0.077573	−11.345	−1.6193	−1.3676	–	−2.6685	–

Table B6. As in Table 3, but for fixed λ.

	R_e	L_X	M_{200}	n	$M_\star$	λ	z
R_e	–	0.25929	0.04714	0.60374	0.63716	–	0.29982
L_X	−3.6471	–	0.21151	−0.080153	0.33863	–	0.51151
M_{200}	−0.29278	−2.5564	–	−0.13082	0.16229	–	0.13857
n	−20.324	−0.58229	−1.1791	–	0.18071	–	−0.0135
$M_\star$	−23.219	−5.9738	−1.6507	−1.9649	–	–	0.47589
λ	–	–	–	–	–	–	–
z	−4.7505	−13.87	−1.2878	−0.070441	−11.859	–	–

Table B7. As in Table 3, but for fixed z.

	R_e	L_X	M_{200}	n	$M_\star$	λ	z
R_e	–	0.1256	0.016817	0.63101	0.58866	0.025858	–
L_X	−1.1086	–	0.34469	−0.12338	0.15958	0.48296	–
M_{200}	−0.089331	−6.1803	–	−0.16127	0.14449	0.44543	–
n	−22.66	−1.0792	−1.6342	–	0.20006	−0.10169	–
$M_\star$	−19.126	−1.6069	−1.3741	−2.3266	–	0.10323	–
λ	−0.14409	−12.24	−10.315	−0.8125	−0.83019	–	–
z	–	–	–	–	–	–	–

APPENDIX C: TABLE SCHEMA

Table C1. Column descriptions for the parameters used in this study (table published electronically).

Column name	Description	Units
SPIDERS_ID	Unique cluster ID from SPIDERS	–
R.A.	Right ascension of BCG	deg
Dec.	Declination of BCG	deg
$z_{\rm BCG,\,spec}$	Spectroscopic redshift of BCG	–
$z_{\rm BCG,\,spec}$_err	Error on spectroscopic redshift of BCG	–
$z_{\rm RM}$	Photometric redshift of cluster red sequence from redMaPPer	–
$z_{\rm RM}$_err	Error on photometric redshift of cluster red sequence from redMaPPer	–
$z_{\rm clus,\,spec}$	Spectroscopic cluster redshift, estimated from biweight of cluster members	–
$z_{\rm clus,\,spec}$_err, u	Upper error bound on spectroscopic cluster redshift	–
$z_{\rm clus,\,spec}$_err, l	Lower error bound on spectroscopic cluster redshift	–
σ_{200}	Velocity dispersion of cluster	km s^{-1}
σ_{200}_err, u	Upper error bound on velocity dispersion of cluster	km s^{-1}
σ_{200}_err, l	Lower error bound on velocity dispersion of cluster	km s^{-1}
N	Number of cluster members used when computing velocity dispersion	–
λ	Cluster richness estimator from redMaPPer	–
$L_{\rm X}/E_{\rm z}$	Cluster X-ray luminosity from *ROSAT*	erg s^{-1}
$\log_{10}[M_{\rm BCG}]$	Stellar mass of BCG	M$_\odot$
$\log_{10}[M_{\rm BCG}]$_err	Error on stellar mass of BCG	dex
$(g-i)$	k-corrected, dust-corrected, $g-i$ colour of BCG, measured in a 30 kpcaperture	–
$(g-i)$_err	Error on $g-i$ colour of BCG	–
$m_{\rm g}$	g-band apparent magnitude from sigma	–
$m_{\rm g}$_err	Error on g-band apparent magnitude from sigma	–
$R_{\rm e,\,g}$	Effective radius of BCG from sigma, g band	arcsec
$R_{\rm e,\,g}$_err	Error on effective radius of BCG from sigma, g band	arcsec
$n_{\rm g}$	Sérsic index of BCG from sigma, g band	–
$n_{\rm g}$_err	Error on Sérsic index of BCG from sigma, g band	–
$b/a_{\rm g}$	Axis ratio from sigma, g band	–
$b/a_{\rm g}$_err	Error on axis ratio from sigma, g band	–
$\theta_{\rm g}$	Position angle from sigma, g band	deg
$\theta_{\rm g}$_err	Error on position angle from sigma, g band	deg
$\chi_{\nu,\rm g}{}^2$	Reduced χ^2, g band	–
$m_{\rm r}$	r-band apparent magnitude from sigma	–
$m_{\rm r}$_err	Error on r-band apparent magnitude from sigma	–
$R_{\rm e,\,r}$	Effective radius of BCG from sigma, r band	arcsec
$R_{\rm e,\,r}$_err	Error on effective radius of BCG from sigma, r band	arcsec
$n_{\rm r}$	Sérsic index of BCG from sigma, r band	–
$n_{\rm r}$_err	Error on Sérsic index of BCG from sigma, r band	–
$b/a_{\rm r}$	Axis ratio from sigma, r band	–
$b/a_{\rm r}$_err	Error on axis ratio from sigma, r band	–
$\theta_{\rm r}$	Position angle from sigma, r band	deg
$\theta_{\rm r}$_err	Error on position angle from sigma, r band	deg
$\chi_{\nu,\rm r}{}^2$	Reduced χ^2, r band	–
$m_{\rm i}$	i-band apparent magnitude from sigma	–
$m_{\rm i}$_err	Error on i-band apparent magnitude from sigma	–
$R_{\rm e,\,i}$	Effective radius of BCG from sigma, i band	arcsec
$R_{\rm e,\,i}$_err	Error on effective radius of BCG from sigma, i band	arcsec
$n_{\rm i}$	Sérsic index of BCG from sigma, i band	–
$n_{\rm i}$_err	Error on Sérsic index of BCG from sigma, i band	–
$b/a_{\rm i}$	Axis ratio from sigma, i band	–
$b/a_{\rm i}$_err	Error on axis ratio from sigma, i band	–
$\theta_{\rm i}$	Position angle from sigma, i band	deg
$\theta_{\rm i}$_err	Error on position angle from sigma, i band	deg
$\chi_{\nu,i}{}^2$	Reduced χ^2, i band	–

This paper has been typeset from a TEX/LATEX file prepared by the author.